# Synthesis, Structure, and Properties of Monazite, Pretulite, and Xenotime

**Lynn A. Boatner**

*Solid State Division*
*Oak Ridge National Laboratory*
*Oak Ridge, Tennessee 37831*

Reprinted From:

REVIEWS in MINERALOGY and GEOCHEMISTRY

Volume 48 2002

*PHOSPHATES:*
*GEOCHEMICAL, GEOBIOLOGICAL, AND MATERIALS IMPORTANCE*

EDITORS:

MATTHEW J. KOHN — *University of South Carolina, Columbia, South Carolina*

JOHN RAKOVAN & JOHN M. HUGHES — *Miami University, Oxford, Ohio*

*Series Editor:* ***Paul H. Ribbe***
*Virginia Polytechnic Institute and State University*
*Blacksburg, Virginia*

MINERALOGICAL SOCIETY of AMERICA

Washington, DC

# 4 Synthesis, Structure, and Properties of Monazite, Pretulite, and Xenotime

**Lynn A. Boatner**

*Solid State Division*
*Oak Ridge National Laboratory*
*Oak Ridge, Tennessee 37831*

## PROPERTIES OF RARE-EARTH-, Sc-, AND Y-ORTHOPHOSPHATES

### General characteristics

Orthophosphate compounds of the type $A(PO_4)$ include the minerals monazite [$RE(PO_4)$ with RE = the light rare-earth ions, e.g., La, Ce, Nd...], xenotime [$Y(PO_4)$, and also incorporating the heavy RE ions], and pretulite [$Sc(PO_4)$]. The name of the mineral monazite is derived from the Greek word *monazein*, "to be solitary," whereas that of xenotime is derived from the Greek words *xenos*, meaning "foreign" and *time*, meaning "honor." The mineral pretulite is named for Pretul Mountain, located in the Fischbacher Alps in Styria, Austria where the mineral was discovered (Bernhard et al. 1998). Pretulite is only the sixth mineral to have been found in which scandium is a major constituent.

The anhydrous rare-earth (RE) orthophosphates can be structurally divided between the light RE-element compounds with the monoclinic monazite structure (space group $P2_1/n$, $Z = 4$) and the heavier RE compounds with the tetragonal (zircon-type) xenotime structure (space group $I4_1/amd$, $Z = 4$). In terms of the crystal chemistry of these two groups of compounds, a primary distinguishing structural feature is the coordination of the RE, Y, or Sc ions. In the monoclinic monazite structure, the RE ion is located in a polyhedron in which it is coordinated with nine oxygen ions. In the tetragonal xenotime structure, the heavier REs, Y, or Sc are located in a polyhedron in which they are coordinated with eight oxygen ions. Scandium orthophosphate is the basic constituent of the recently identified mineral, pretulite, which belongs to the orthophosphate group with the tetragonal xenotime structure (Bernhard et al. 1998).

Both monazite and xenotime are relatively widely distributed as microcrystalline (or small crystalline) accessory inclusions in granitic rocks, rhyolites, pegmatites, and gneisses. Monazite also occurs in carbonatites, charnockites, migmatites, and quartz veins (Rapp and Watson 1986) as well as in alluvial deposits, including beach sands (e.g., the black beach sands of Kerala, India and beach sands in San Mateo County, California). These alluvial deposits and beach sands are produced by the weathering of peraluminous granites, granitic pegmatites, and other host rock types. The occurrence of the alluvial deposits of monazite and their derivation from the weathering of granitic rocks attest to the ability of the mineral to survive metamorphic and sedimentary cycles that can extend over several hundred million years (Rapp et al. 1987).

### Chemical composition

Natural monazite contains not only cations of the light rare-earth elements, but it also incorporates uranium and thorium. Monazite is the principal ore for the commercial extraction of thorium, and it has also been used as a secondary source of uranium. Monazite deposits are located in the United States, Australia, South Africa, Sri Lanka, Brazil, India, Malagasy, and Canada. As shown in Table 1, monazite is capable of incorporating significant amounts of both uranium and thorium (Boatner and Sales 1988, Houk 1943). Because of the chemical durability of monazite, relatively harsh chemical

1529-6466/00/0048-0004$05.00

treatments at elevated temperatures are required for the extraction of thorium or uranium. One method of extraction consists of treatment in 45% sodium hydroxide at 138°C, and a second commercial extraction process consists of subjecting the ore to a 93% solution of sulfuric acid at 210°C.

**Table 1.** Composition of natural monazites.

| *Mineral source* | *$UO_2$ (wt %)* | *$ThO_2$ (wt %)* | *Combined lanthanide oxides (wt %)* | *Other oxides (wt%)* | *$P_2O_5$ (wt %)* |
|---|---|---|---|---|---|
| Piona, Italy[a] | 15.64 | 11.34 | 35.24 | 6.76 | 31.02 |
| Ratunapura, Sri Lanka[b] | 0.10 | 14.32 | 53.51 | 5.03 | 26.84 |
| Burke County,[c] N.C. | 0 | 6.49 | 62.26 | 1.97 | 29.28 |
| Brazil[d(1)] | N.D, | 10.05 | 58.13 | 6.98 | 25.51 |
| Malay[d(2)] | N.D. | 8.38 | 60.98 | 6.43 | 23.92 |
| Australia[d(3)] | N.D. | 3.80 | 65.40 | 3.94 | 26.89 |
| India[e] | N.D. | 10.22 | 60.36 | 3.23 | 26.82 |

[a] Gramaccioli & Segalstad (1978)
[b] Kato T (1958)
[c] Penfield SC (1882)
[d] Houk LG (1943) Monazite Sand. *Information Circular IC 7233*, U S Dept of the Interior-Bureau of Mines
[d(1)] monazite from the river sands of Rio Paraguassir in Bahia, Banderiro do Mello.
[d(2)] concentrated monazite from the Sempang Tin Co., Pahang, Malay Peninsula.
[d(3)] monazite from Cooglegong and Moolyella, Western Australia.
[e] Johnstone SJ (1914)

The extensive and detailed analytical results given in Table 1 of Förster (1998a) illustrate the extreme compositional diversity exhibited by natural monazites. In fact, Förster has even reported the existence of a monazite–group mineral that is intermediate between monazite and huttonite. Förster's analysis indicated that complete miscibility exists between common monazite-(Ce) and the phosphate mineral brabanite [Ca,Th,U$(PO_4)_2$]. The monazite/xenotime compositional systematics have also been examined by Heinrich et al. (1997). Additional data related to the compositional diversity of monazites can be found in the work of Bea (1996), Bea et al. (1994), and Hinton and Patterson (1994).

The large compositional variability that can be exhibited by natural xenotime is illustrated by the results of Förster (1998b), who analyzed xenotime specimens from various peraluminous granites found in Erzgebirge, Germany. This work showed that, with respect to the heavy rare earths as well as Y, U, and Th, a wide range of xenotime compositions occurs. Specifically, xenotime grains normally obtained from granites worldwide are characterized by compositions consisting of 70 to 80 mol % $Y(PO_4)$ + 16 to 25 mol % heavy rare-earth phosphates. Förster (1998b) found specimens of xenotime with as much as 45 mol % heavy rare-earth ions replacing yttrium.

The new mineral pretulite represents a scandium-dominant analog of xenotime-(Y). Bernhard et al. (1998) determined an empirical formula of [$Sc_{0.98}Y_{0.02}(PO_4)$] for pretulite obtained from the Styrian lazulites. They reported a range of Y content replacing Sc [i.e., Y/(Y + Sc)] in the range of 0.5 to 3.2 mol %; traces of the heavy rare-earth elements Yb, Er, and Dy were also found. The composition of pretulite was reported to be inhomogeneous on a micron scale due to variations in yttrium content of 0.39 to 2.49 wt %.

Monazite, xenotime, and pretulite, in addition to minerals such as purpurite [$Mn(PO_4)$] and lithiophylite [$LiMn(PO_4)$], represent members of a relatively small group of phosphate minerals that are classified as anhydrous and as "lacking foreign anions." Hydrated modifications of these substances, including rhabdophane-type phosphates [$RE(PO_4)\cdot nH_2O$, with RE = La to Tb], weinschenkite-type phosphates [$RE(PO_4)\cdot 2H_2O$ with RE = Dy, Y, Er, Yb, or Lu], the orthorhombic compound $Dy(PO_4)\cdot 1.5H_2O$, and other hydrated phosphates such as the pseudo-hexagonal, orthorhombic mineral ningyoite [$(Ca,U,RE)(PO_4)\cdot xH_2O$; Muto et al. 1959) can be synthesized at reduced temperatures and are well known. Recently, the yttrium-based rhabdophane-type compounds $Y(PO_4)\cdot 0.8H_2O$ and $Er(PO_4)\cdot 0.9H_2O$ have also been synthesized and investigated by Hikichi et al. 1989. A hydrated form of $Sc(PO_4)$ occurs in nature as kolbeckite [$Sc(PO_4)\cdot 2H_2O$] – a mineral of supergene or hydrothermal derivation. An irreversible structural transformation of rhabdophane-to-monazite or rhabdophane-to-xenotime can be achieved by heating the hydrated phosphate compounds. The transformation involves an initial dehydration in the range of ~100 to 400°C to produce a hexagonal form of the $A(PO_4)$ compound, followed by a structural transformation that occurs exothermically in the range of 500-900°C – depending on the specific cation (Jonasson and Vance 1986, Hikichi et al. 1988, 1996). Hikichi et al. (1978) have noted that the dehydrated hexagonal form of the RE orthophosphates will readily re-hydrate when exposed to air at ambient temperature. The mechanochemical preparation (i.e., by grinding in various media) and the conversion of various types of hydrated $RE(PO_4)$ and $Y(PO_4)$ compounds have been described in detail by Hikichi et al. (1989, 1991, 1993, 1995, 1996).

**Chemical durability**

The anhydrous RE, Y, and Sc orthophosphates are compounds that are extremely insoluble and chemically durable in an aqueous environment over a relatively wide pH range (Sales et al. 1983). In particular, the chemical durability of monazite is indicated by the extreme treatments, noted in the previous section, that are required to extract thorium from natural ores. Some alteration of monazite does occur, however, under hydrothermal conditions, and the responsible mechanisms and geochemical implications of these alteration processes have been studied in detail by Poitrasson et al. 1996. Subsequent investigations of the behavior of monazite under hydrothermal conditions and the relevance of this behavior to U-Pb isotope systematics and the associated geochronological implications have been carried out by Teufel and Heinrich (1997). These workers reported only minor surface dissolution effects in the case of monazite grains, but more significant alterations of monazite powders were observed. Specifically, Teufel and Heinrich found a temperature-dependent loss of lead from monazite powders exposed to hydrothermal conditions. Andrehs and Heinrich (1998) and Gratz and Heinrich (1997) have hydrothermally synthesized and investigated (RE+Y)-orthophosphate solid solutions. They produced both monazite- and xenotime-structure phases and demonstrated the utility of the temperature-dependent partitioning of the rare earths between monazite and xenotime as a method of geothermometry. Additional hydrothermal investigations have been carried out by Podor and Cuny (1997). Surface reactions (including replacement reactions) of synthetic monazite- and xenotime-structure RE-orthophosphates in various environments have been also investigated by Jonasson et al. (1988).

**Radiation damage effects**

As previously noted, monazite usually contains significant amounts of thorium as well as uranium, and xenotime also contains uranium. Naturally radioactive minerals are, therefore, exposed to displacive radiation damage events over geological time scales. Accordingly, such minerals are frequently found in the metamict state, i.e. they can

exhibit external faceting and the appearance of a crystal, but they have been rendered structurally amorphous by cumulative radiation damage effects. The issue of the metamictization of natural monazite has been examined in the early structural work of Ghouse (1968), who examined the effects of heating on monazites from Kerala beach sands. Ghouse found only a small difference in the structure of the natural monazite specimens that he examined following heat treatments up to 1130°C. More recently, Ewing (1975) and Ewing and Haaker (1980) have noted that monazite is, in fact, generally always found in a highly crystalline (i.e., not fully metamict) form despite being subjected to displacive radiation damage over hundreds of millions to billions of years. This represents an important issue for mineral phases such as monazite that are considered as host waste forms for the disposal of actinides and other types of high-level radioactive waste. The concern is that, in such an application, structural alterations leading to amorphization will render the waste form less chemically durable and more susceptible to the loss of radioactive ions by dissolution or leaching in aqueous media (Eyal and Kaufman 1982, Eyal and Fleischer 1985, Roy and Vance 1981). The subject of radiation damage effects and their impact on the performance of radioactive waste forms is thoroughly reviewed by Ewing and Wang (this volume), and the subject is very well referenced in their chapter. In brief, however, the original idea that monazite was simply very resistant to radiation damage and thus did not experience metamictization has been found to be incorrect. The material is easily amorphized by displacive radiation events but it also recovers its ordered structure by annealing processes that occur at relatively low temperatures. This issue has recently been well resolved and placed on solid ground by the work of Meldrum et al. (1997a,b,c, 1998, 2000). One additional interesting point is that, in the case of the rare-earth orthophosphates, Sales et al. (1983) found that even in the radiation-damaged phase of a monazite matrix the dissolution rate remained quite low.

**Thermophysical and thermochemical properties**

Monazite, xenotime, and (presumably) pretulite in their stable anhydrous forms are refractory materials with reported melting points in excess of 2000°C (Bondar 1976, Rouanet et al. 1981, Hikichi and Nomura 1987). In the case of natural monazite from Nogisawa-mura, Japan, Hikichi and Nomura (1987) used a solar furnace to measure a melting temperature of 2057(±40)°C. These orthophosphate compounds remain relatively stable chemically until near or at their melting point, where some thermal decomposition is initiated that is apparently associated with the loss of phosphorous-containing species. Table 2 lists the melting point of various phase-pure RE orthophosphates and synthetic xenotime as determined by Bondar (1976) and Hikichi and Nomura (1987). It should be noted that there are significant differences between the earlier values for the melting points reported by Bondar and the more recent results of Hikichi and Nomura.

The thermochemical properties of the rare-earth orthophosphates [plus $Sc(PO_4)$ and $Y(PO_4)$] have recently been investigated in detail by Ushakov et al. (2001). These workers obtained the formation enthalpies of 14 orthophosphates by using calorimetric techniques and found an almost linear dependence between the enthalpies of formation and the rare-earth radius, from $La(PO_4)$ (-321.4 kJ/mol) to $Lu(PO_4)$ (-236.9 kJ/mol); xenotime and pretulite were found to be consistent with this behavior as well. The structural transition from the xenotime structure to the monazite structure was not manifested in a significant discontinuity in the relatively linear trend in the enthalpies of formation. The complete results of these detailed thermochemical studies are tabulated in Ushakov et al. (2001).

**Table 2.** Melting points of rare-earth- and Y-orthophosphates.

| *Compound* | *Melting point (°C)* | *Liquid spectral emissivity* [a] *(at 0.65 μm)* |
|---|---|---|
| $La(PO_4)$ | 2072 (20)[a] | 1.00 |
| | 2300 [b] | |
| $Ce(PO_4)$ | 2045 (20)[a] | 0.99 |
| $Pr(PO_4)$ | 1938 (20)[a] | 0.82 |
| $Nd(PO_4)$ | 1975 (20)[a] | 0.85 |
| | 2250 [b] | |
| $Sm(PO_4)$ | 1916 (20)[a] | 0.90 |
| $Eu(PO_4)$ | 2200 [b] | |
| $Gd(PO_4)$ | 2200 [b] | |
| $Tb(PO_4)$ | 2150 [b] | |
| $Dy(PO_4)$ | 2150 [b] | |
| $Er(PO_4)$ | 1896 (20)[a] | 1.00 |
| | 2150 [b] | |
| $Yb(PO_4)$ | 2150 [b] | |
| $Y(PO_4)$ | 1995 (20)[a] | 1.00 |
| | 2150 [b] | |

(a) Hikichi and Nomura (1987)
(b) Bondar et al. (1976)

## CRYSTAL GROWTH OF MONAZITE, PRETULITE, AND XENOTIME

To date, pretulite has only been found in lazulite and quartz-rich domains (Bernhard et al. 1998), and euhedral pretulite crystals up to a maximum size of ~200 μm were observed. Large crystals of monazite weighing up to ~25 kg have been reported; however, natural xenotime crystals are more limited in size relative to monazite. One of the larger known xenotime crystals, as represented by a specimen from a pegmatite (Minas Gerais, Brazil), is ~4.2 cm tall and is presently housed in the Natural History Museum in Los Angeles, California. Regardless of their size, natural crystal specimens of these minerals are generally characterized by compositional variations (monazite, of course, being a mixed rare-earth orthophosphate by origin), by structural defects, and radiation damage effects (because most monazites contain thorium and uranium, and xenotime frequently contains uranium.) Additionally, the sample histories of these minerals in the geological environment and the alteration conditions to which they have been subjected are not known with certainty. Because of the limitations of natural mineral specimens in terms of purity, compositional variation, crystal perfection, and the availability of appropriate well-characterized naturally occurring specimens, synthetic high-purity (or controlled purity) single crystals of monazite, xenotime, and pretulite are essential for fundamental studies of the structural characteristics, solid state chemistry, thermochemistry, and physical properties of the pure orthophosphate phases. In many cases, synthetic single crystals are also necessary for use in the practical applications outlined elsewhere in this chapter. The following sections detail studies on the synthesis of such specimens.

### Flux growth of RE-, Sc-, and Y-orthophosphates

A crystal growth technique similar to that originally described by Feigelson (1964) has been used to grow phase-pure single crystals of all of the RE-orthophosphates [except for the radioactive member $Pm(PO_4)$]—including the end members, $La(PO_4)$ and $Lu(PO_4)$, as well as $Y(PO_4)$ and $Sc(PO_4)$. This growth method has been applied to the

preparation of orthophosphate-host single crystals doped with controlled amounts of iron-group, other RE, actinide, and other (e.g., Zr and Hf) impurities. Additionally, the technique has been used to grow mixed "alloy" rare-earth orthophosphate single crystals for use in x-ray diffraction structural refinement studies, the results of which are described elsewhere in this chapter.

The growth of the subject orthophosphate single crystals is carried out by means of a high-temperature solution (or flux) growth process using lead pyrophosphate $Pb_2P_2O_7$ as the high-temperature solvent (Wickham 1963, Wanklyn 1972). The flux is prepared by first chemically precipitating lead hydrogen phosphate from a lead nitrate solution through the addition of phosphoric acid. The resulting $PbH(PO_4)$ precipitate is subsequently oven dried in air. The lead hydrogen phosphate is then combined with the appropriate RE oxide plus any desired dopant oxides, and the mixture is placed in a platinum crucible and covered with a loose-fitting Pt lid. In a typical small laboratory-scale growth (e.g. in a 50 ml Pt crucible), 60 g of $PbHPO_4$ would be combined with 3.5 g of $RE_2O_3$. The growth crucible is placed in a temperature-controlled and programmable resistance-heated furnace and heated to 1360°C. During the initial heating phase, the lead hydrogen phosphate decomposes to form $Pb_2P_2O_7$, which then reacts at elevated temperatures to form the RE, Y, or Sc orthophosphate. The unreacted excess Pb pyrophosphate then serves as a high-temperature solvent in which the orthophosphate is dissolved. Following a 1360°C "soaking period," the duration of which can be varied from several hours to several days, the furnace is cooled at a linear rate of 0.5 to 2.0°C per hour to ~900°C. Below this temperature, the crystal growth does not proceed further, and thus the furnace is rapidly cooled to room temperature. Figure 1 illustrates the Pt crucible and contents following the crystal growth of synthetic pretulite, $Sc(PO_4)$. The faceted $Sc(PO_4)$ crystals have nucleated on and are located around the periphery of the crucible and have formed on the surface of the white $Pb_2P_2O_7$ flux that occupies the remainder of the solidified surface as shown in Figure 1. In this case, the long dimension of the largest $Sc(PO_4)$ crystal is ~2.0 cm.

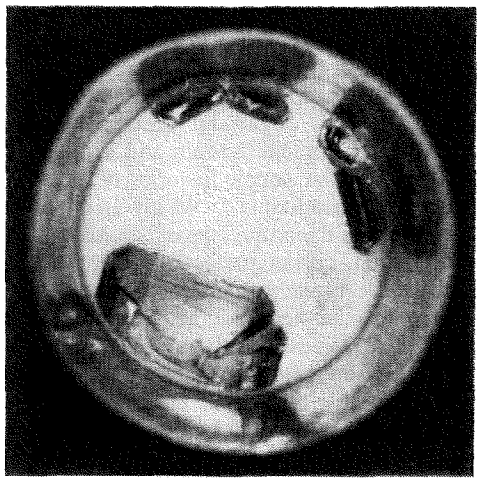

**Figure 1.** Single crystals of synthetic pretulite [pure $Sc(PO_4)$] are shown inside a 50 ml Pt crucible following a high-temperature-solution (flux) growth run. The large white central area is solidified $Pb_2P_2O_7$ flux, and the $ScPO_4$ crystals have nucleated and grown around the periphery of the Pt crucible. A normal flux-growth run takes ~30 days, and an additional ~30 days is required to chemically remove the $Sc(PO_4)$ crystals from the solidified flux. The outer diameter of the Pt crucible is ~3.9 cm.

As illustrated in Figure 1, the orthophosphate single crystals that are grown by means of the spontaneous-nucleation, flux-growth technique are initially entrained in the solidified $Pb_2P_2O_7$ flux upon cooling to room temperature. This entraining can be minimized by an elevated-temperature decanting of the molten flux prior to the final cooling step. In some cases, however, (e.g., when one of the tetragonal crystals grows completely across the diameter of the crucible), this subjects the phosphate crystals to thermomechanical stresses that may induce fracture. An example of a large (originally ~3 cm long) $Y(PO_4)$ crystal that fractured on removal from the flux is illustrated in Figure 2.

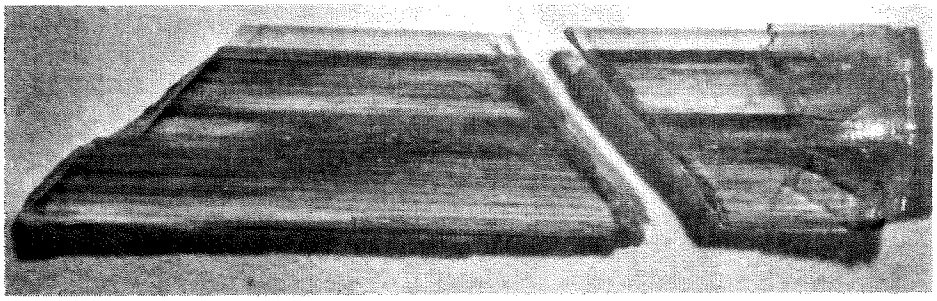

**Figure 2.** A flux-grown single crystal of synthetic xenotime [pure $Y(PO_4)$] is shown following its removal from a 50 ml Pt crucible. This "bar-like" form is typical of the growth habit of the tetragonal rare-earth and Y orthophosphates. The four-fold symmetry axis of the tetragonal structure lies along the long dimension of the "bar." Growth striations that frequently occur on the surface of the flux-grown tetragonal-structure orthophosphate crystals are evident. The crystal has fractured on cooling due to thermomechanical stresses. The horizontal dimension is ~3.5 cm.

This figure also illustrates the surface striations that are often observed, the long dimension of which lies along the tetragonal *c* axis. A more benign but significantly slower method for removing the solidified flux is to place the crucible and its contents in boiling nitric acid. Even under this somewhat extreme condition, the solubility of the solidified $Pb_2P_2O_7$ is sufficiently low that a period of four-to-five weeks may be required to completely free the phosphate crystals and remove any residual pyrophosphate flux (including flux inclusions with open porosity exposure.) Accordingly, in those cases where the maximum size crystals are not required for a given experimental investigation, the flux-decanting method provides a more expedient means of obtaining crystal samples. In this regard, a special technique and apparatus for decanting the flux from a number of Pt growth crucibles simultaneously has been described by Smith and Wanklyn (1974). This apparatus had a relatively large thermal mass so that the crucibles cooled more slowly than in the case of simply removing an individual Pt crucible with tongs and decanting the flux into a hollow firebrick or a nickel boat filled with alumina powder. This feature undoubtedly accounts for the observation of Smith and Wanklyn (1974) that by using the hot-pouring device that they describe, the orthophosphate (or orthovanadate) crystals could be recovered without any evidence for thermal shock or mechanical damage. Tanner and Smith (1975) have examined the perfection of single crystals of $Tb(PO_4)$, $Dy(PO_4)$, $Ho(PO_4)$, and $Yb(PO_4)$ that were grown by slow cooling (i.e., spontaneous nucleation) using a $Pb_2P_2O_7$ flux. These workers found that, in the case of optically-clear samples, the average dislocation density was $\sim 10^4$ $cm^{-2}$, whereas large dislocation-free areas were found in the case of crystals that formed as thin plates. These workers employed a hot pouring (straining) technique to recover the crystals, and they observed cracking and dislocation loops originating from the edges of the crystals as well as evidence for plastic deformation that had apparently occurred after the growth was complete.

**RE-, Sc-, and Y-orthophosphate crystal morphology**

In the case of the monoclinic rare-earth orthophosphates grown using the method outlined above, the crystals generally grow with two habits that are morphologically quite different. Rappaz et al. (1981a,b) have determined the relationship between the growth faces of the monoclinic crystals and the *b* axis using precession methods. Figure 3 illustrates the two monoclinic crystal morphological forms as exemplified by $La(PO_4)$ and $Eu(PO_4)$ and the relation of the observed crystal faces to the *b*-axis. The monoclinic orthophosphates, $Ce(PO_4)$, $Pr(PO_4)$, and $La(PO_4)$, are more frequently characterized by the growth habit illustrated on the left of Figure 3, whereas $Nd(PO_4)$, $Sm(PO_4)$, and $Pr(PO_4)$ are frequently characterized by the morphology shown at the right of Figure 3. Occasionally, a third monoclinic growth habit that (not shown in Fig. 3) is observed in which the crystals consist of thin, flat {010} plates, the edges of which form the monoclinic angle of the crystal structure.

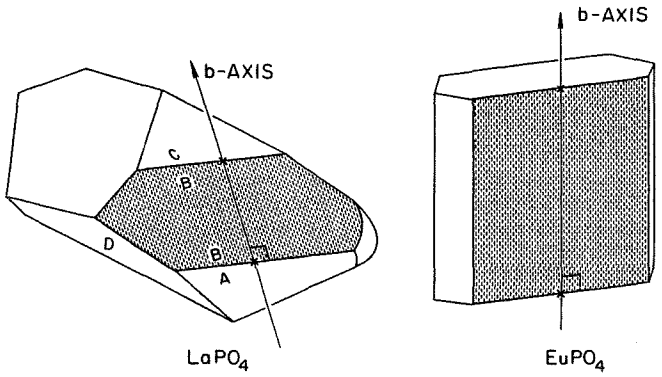


**Figure 3.** Single-crystal habits for monoclinic rare-earth orthophosphates grown from a $Pb_2P_2O_7$ flux. The relationship between the monoclinic crystal *b*-axis and the crystal faces for the two morphologies is indicated. In some cases, a third habit (not shown) occurs that consists of thin, diamond-shaped plates whose angles are determined by the monoclinic angle β (after Rappaz et al. 1981a).

With the exception of $Sc(PO_4)$, all of the tetragonal orthophosphates grow with a rectangular parallelepiped habit like that shown in Figure 2 for $Y(PO_4)$. The long dimension of the crystals lies along the tetragonal *c*-axis. The orthophosphate crystals generally nucleate and grow as elongated {001} plates on the top surface of the $Pb_2P_2O_7$ flux. Smaller crystals frequently exhibit tetragonal prism forms and pyramid-capped ends, but the larger crystals usually grow faster parallel to the $Pb_2P_2O_7$ nutrient liquid surface so that the dimension (thickness) of the face in the direction perpendicular to the flux surface is smaller. The growth habit of flux-grown single crystals of $Sc(PO_4)$ is generally not in the form of elongated bars but is more compact as exemplified by the large faceted scandium orthophosphate crystal shown in Figure 1.

**Impurities and dopant incorporation**

In the case of growth in a $Pb_2P_2O_7$ solvent, some level of contamination by lead is anticipated, and does in fact occur –particularly in the case of $Ce(PO_4)$. Low-level trivalent lead impurities were observed in $Y(PO_4)$ by Abraham et al. (1980a) and investigated using electron paramagnetic resonance (EPR) spectroscopy. Figure 4 illustrates the EPR spectrum due the $Pb^{3+}$ "even" isotopes, along with EPR lines due to $Fe^{3+}$ and $Gd^{3+}$ impurities. More recently, the nature and dependence of the Pb content

that is present in orthophosphate crystals grown using a $Pb_2P_2O_7$ flux has been studied quantitatively by Donovan et al. (2002a,b). These studies were undertaken as a result of the currently widespread use of flux-grown RE, Y, and Sc orthophosphate single crystals as microprobe analytical standards for rare-earth, Y, and Sc analysis (Jarosewich and Boatner 1991). The analytical results of Donovan et al. (2002a,b) showed that none of the xenotime-structure orthophosphates [$Y(PO_4)$, $Sc(PO_4)$ or Gd-$Lu(PO_4)$] contained appreciable amounts of Pb. Only the monoclinic-structure compounds $Ce(PO_4)$ [and possibly $La(PO_4)$ and $Sm(PO_4)$] were found to contain Pb in a concentration sufficient to result in a 2 to 4% variance in composition.

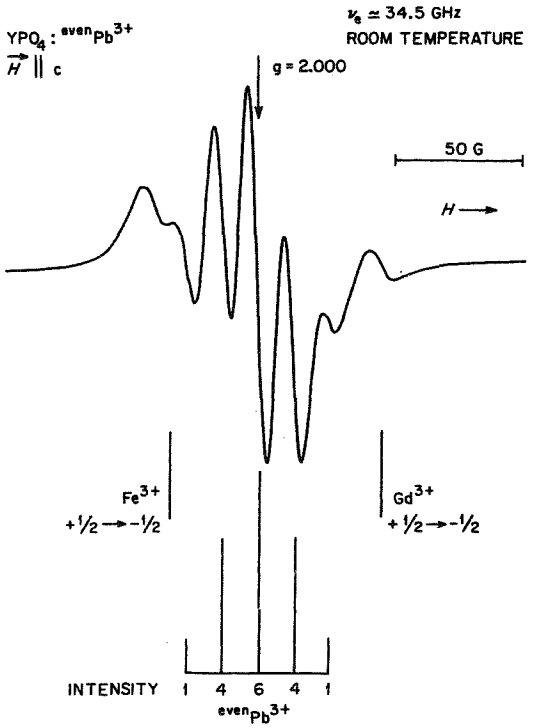


**Figure 4.** The electron paramagnetic resonance (EPR) spectrum of $Y(PO_4)$ (obtained with the applied magnetic field along the crystal *c*-axis) shows signals from the "even" isotopes of Pb that exhibit a superhyperfine structure due to interactions with four equivalent $^{31}P$ ($I = 1/2$) neighbors. Also shown are EPR lines due to impurities of $Fe^{3+}$ and $Gd^{3+}$. EPR lines due to $^{207}Pb$ are also observed in the full spectrum, but are not shown here. Low levels of Pb impurities are incorporated in orthophosphate single crystals grown from a $Pb_2P_2O_7$ flux, but the concentration levels are significant mainly in the case of $Ce(PO_4)$ and not in the case of the tetragonal-structure orthophosphates (after Abraham et al. 1980a).

The tetragonal RE, Y, and Sc orthophosphates in particular have been widely used as host media for a variety of solid state chemical, spectroscopic, magnetic resonance, neutron and other studies of rare-earth and actinide impurities. These materials have proved to be ideal hosts for the incorporation of other rare-earth dopants (e.g., Er-doped $Lu(PO_4)$ for microlaser studies). Doped orthophosphates with desired levels of dopants are desirable for both basic investigations and applications. Unfortunately, there are apparently no available quantitative data on the segregation coefficients for the rare earths in the tetragonal orthophosphates.

Experience has shown that the lighter rare earths may be rejected to a significant degree during the flux growth of the heavier RE orthophosphates such as $Lu(PO_4)$. In practice, it has proven difficult, for example, to incorporate more than 1.0% Ce in $Lu(PO_4)$. In the case of doped orthophosphate crystals, the actual dopant concentration is usually determined by quantitative analysis subsequent to crystal growth by using techniques such as glow-discharge mass spectrometry. In the case of the growth of orthophosphate single crystals that are doped with radioactive actinide elements, special glove-box containment facilities are used because of the alpha activity of these materials. In previous work, the method described here for orthophosphate single-crystal growth by utilizing a high-temperature solvent has been applied to the preparation of U-, Np-, Pu-, Am-, Cm-, and Cf-doped specimens. These unique materials have been the subject of a wide range of fundamental solid state chemical studies (Murdoch et al. 1996, Sytsma et al. 1995, Kot et al. 1993a,b; Abraham et al. 1980a,b, 1982, 1985, 1987; Liu et al. 1997, 1998; Kelly et al. 1981, Huray et al. 1982).

**Orthophosphate crystal size and alternate growth methods**

The single crystal of synthetic xenotime shown in Figure 2 represents the approximate practical size limit achieved during numerous laboratory-scale spontaneously-nucleated flux crystal growths carried out over a period of ~20 years. The flux crystal growth approach is extremely useful for producing research specimens with various doping levels, compositions, etc., because eight or more growth runs in 50 ml Pt crucibles can be carried out simultaneously in a laboratory-size box furnace. The relatively recent identification of a variety of practical applications for the tetragonal-symmetry orthophosphates, however, has created a need for the controlled growth of larger single crystals of these materials. Unfortunately, attempts to grow large crystals of, for example, $Lu(PO_4)$ from the melt in iridium crucibles have not been successful because these materials do not melt congruently and exhibit some decomposition at the melting temperature. This leaves, as alternative growth methods, either hydrothermal growth, like that used to commercially grow single crystals of berlinite [$Al(PO_4)$], or top-seeded solution growth—a more sophisticated variant of high-temperature solution growth. Using the latter, Eigermann et al. (1978) have previously determined the solubility curves for $Lu(PO_4)$, $Yb(PO_4)$, $Tm(PO_4)$, $Er(PO_4)$, $Ho(PO_4)$, $Dy(PO_4)$, $Tb(PO_4)$, and $Yb(PO_4)$ in $Pb_2P_2O_7$. These results are illustrated in Figure 5. Additionally, these workers determined the saturation temperatures of various concentrations of $Y(PO_4)$ in $Pb_2P_2O_7$ to which varying amounts of PbO were added and found that the solubility increased with increasing PbO content in the flux. The growth of rare-earth orthophosphate crystals from a lead-phosphate flux consisting of various mixtures of PbO and $P_2O_5$ has also been investigated by Wanklyn (1978). The data of Eigermann et al. (1978) and Wanklyn (1978) are particularly valuable in regard to the application of top-seeded-solution growth to the tetragonal rare-earth and yttrium orthophosphates. Top-seeded-solution crystal-growth studies of the tetragonal-symmetry orthophosphates are currently ongoing in at least two laboratories. Finally, Hintzman and Müller-Vogt (1969) have described a variation of the flux growth technique in which a relatively small oscillating temperature that is superimposed on the normal linear cooling rate used during standard flux growth is employed. As indicated by the size of the crystals obtained by means of the oscillating temperature method, as shown in the work of Hintzman and Müller-Vogt, there is no apparent advantage to this approach. Finally, a method for the transfer and growth of single crystals of $Ho(PO_4)$ has been described by Orlovskii et al. (1975). In this relatively unusual approach, the authors found that the crystal-growth habit strongly depended on the crystallization temperature, and they were able to grow $Ho(PO_4)$ crystals as a dipyramid, dipyramid with prism face, columnar, and blade-like crystals.

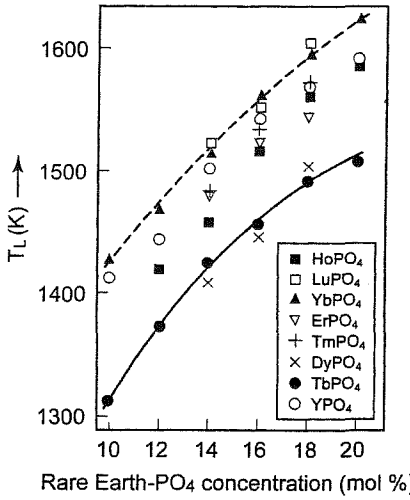


**Figure 5.** The solubility curves of the rare-earth orthophosphates in $Pb_2P_2O_7$ are shown [plotted from the data of Eigermann et al. (1978)]. The solubility data are plotted for $Lu(PO_4)$, $Yb(PO_4)$, $Tm(PO_4)$, $Er(PO_4)$, $Ho(PO_4)$, $Dy(PO_4)$, $Tb(PO_4)$, and $Y(PO_4)$. The solubility shows a decrease with increasing atomic number of the rare-earth elements, although the differences in solubility between neighboring elements are relatively small.

## CHEMICAL SYNTHESIS OF MONAZITE, PRETULITE, AND XENOTIME

### Urea precipitation

A method has been described by Abraham et al. (1980b) that can be used to synthesize all of the rare-earth orthophosphates, plus $Y(PO_4)$ and $Sc(PO_4)$, in powder form and that exercises a relatively high degree of control over the particulate size. This process has proven to be extremely useful and versatile in the preparation of high-purity, stoichiometric orthophosphate powders for use in a wide range of investigations, including studies of sintering and compaction, x-ray diffraction determinations of orthophosphate thermal expansion coefficients, and the preparation of doped cathodoluminescent phosphors.

In the urea synthesis and precipitation process illustrated schematically in Figure 6, the RE oxides are converted into the orthophosphate form by first dissolving a given oxide in a hot nitric acid solution. Through the addition of ammonium dihydrogen phosphate to the solution, a metathesis reaction is initiated that forms the RE, Y, or Sc orthophosphate. To carry out the controlled precipitation process that yields a uniform particle size, urea $[(NH_2)_2CO]$ is added in a granular form, and the resulting mixture is heated at ~180°C until the orthophosphate precipitate begins to form. Upon further heating in a fume hood to ~400°C, ammonia, nitrogen, hydrogen, water vapor, and $CO_2$ are evolved. At this point, the material is transferred to an alumina crucible and a final calcination is carried out between 800 and 850°C. Larger amounts of urea correspond to the formation of smaller orthophosphate particles in the resulting powder. Abraham et al. (1980b) employed up to a 720:1 mole ratio of urea to orthophosphate and were able to produce relatively monodispersed, sub-micron $Ce(PO_4)$ powders. As indicated in the flow chart shown in Figure 6, the powders produced by controlled precipitation from urea can be used to form high-density orthophosphate ceramic bodies by hot pressing or by standard cold pressing and sintering methods. Using powder formed by this approach, Abraham et al. (1980b) were able to produce orthophosphate ceramics with up to 97% of

the theoretical density by hot pressing at 1100°C at 280 bar (4000 psi) for one hour. Floran et al. (1981a,b) also investigated the use of orthophosphate powders synthesized by urea precipitation to form synthetic monazite ceramics by employing both hot pressing and cold pressing followed by sintering.

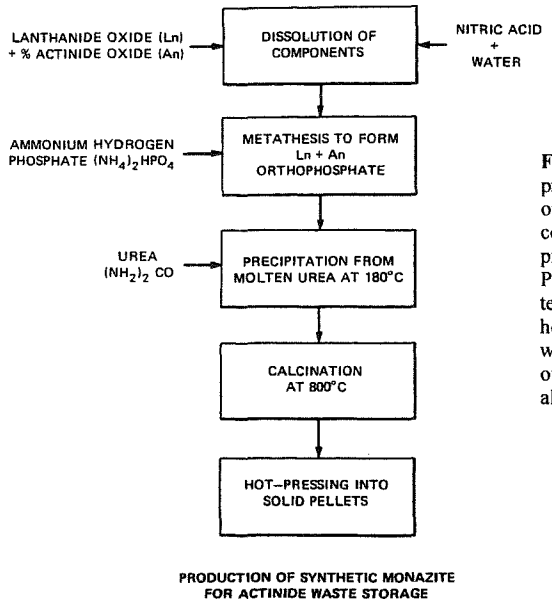


**Figure 6.** Flow diagram for the preparation of rare-earth, Y, and Sc orthophosphate powders with controlled particle size by means of precipitation from molten urea. Powders synthesized by this technique have been compacted by hot pressing to form ceramic bodies with >97% of the theoretical density of the compound (after Abraham et al. 1980b).

In the case of urea-precipitation-synthesized $Ce(PO_4)$ powder, Floran et al. (1981a) produced a ceramic microstructure consisting of large uniaxially-oriented cryptocrystalline grains by hot pressing at 340 bar for 1 hour at 1000°C. The urea precipitation process was also employed by Petek et al. (1982) to synthesize mixed rare-earth orthophosphates that contained a diverse suite of iron-group and other cations (i.e., either cations found in simulated light water reactor wastes or in Savannah River defense waste). By using the urea precipitation process, Petek et al. were able to synthesize $La(PO_4)$ powders that contained up to 10 wt % of chemically simulated light water reactor waste. These powders were subsequently compacted using both cold pressing and sintering or hot pressing (4000 psi, 1050°C, 1 h), and in both cases, ceramic bodies with a density of 96% of theoretical were obtained, and no phases other than the monoclinic monazite phase were observed. Additionally, in their studies of the chemical durability of monazite loaded with Cs, Sr, or U, Sales et al. (1983) employed the urea precipitation process to synthesize doped $La(PO_4)$ precursor powders that were subsequently compacted using hot pressing to produce standard high-density samples for leach testing in aqueous media. The preparation of chemically diverse light rare-earth-element orthophosphates by means of urea precipitation and studies of the subsequent formation of high-density ceramic bodies by various compaction methods have been reviewed and summarized previously in some detail by Boatner and Sales (1988).

### Metathesis reactions with $BPO_4$

Rare-earth orthophosphates and the actinide phosphates $Pu(PO_4)$ and $PuP_2O_7$ have been synthesized using a process developed by Bamberger (1982) and Bamberger et al. (1984) that consists of a metathesis reaction with boron phosphate $B(PO_4)$. Bamberger first synthesized $B(PO_4)$ by heating mixtures of $H_3(PO_4)$ and $H_3BO_3$ to 1000°C in air.

Subsequently, the $B(PO_4)$ was mixed with the rare-earth oxide and heated in a Pt boat at temperatures up to 1000°C. In the case of the formation of $Ce(PO_4)$, the metathesis reaction proceeded according to the relation:

$$CeO_2 + B(PO_4) \rightarrow Ce(PO_4) + 1/2\ (B_2O_3) + 1/4\ (O_2)\ .$$

The evolution of oxygen in this reaction was reported to occur in the range of 550 to 600°C. A metathesis reaction using $B(PO_4)$ was also shown to be effective in producing rare-earth orthophosphates starting with the trifluoride form of the rare earth, and this reaction proceeded according to the relation:

$$NdF_3 + B(PO_4) \rightarrow Nd(PO_4) + BF_3\ .$$

Bamberger also applied a similar metathesis reaction process to the synthesis of phosphates of uranium and neptunium, thus this represents a versatile and alternative synthesis method for the conversion of rare-earth oxides or halides to the phosphate form.

**Solid state reactions**

Hikichi (1991) and Hikichi et al. (1978, 1980) have reported the solid state synthesis of the orthophosphates of La, Ce, Pr, Nd, Sm, Gd, Y, Dy, Er, and Yb by heating the rare-earth trichloride $RECl_3$, oxide $RE_2O_3$, $CeO_2$ or $Ce(NO_3)_3$ with either $(NH_4)_2H(PO_4)$, $K_2H(PO_4)$, $Na_2H(PO_4)$, or $H_3(PO_4)$, with an atomic ratio of one phosphorous per rare earth. In this process, the RE and phosphorous-containing compounds were mixed and initially dried for one day at 100°C. The material was subsequently heated in a Pt crucible from 200 to 1000°C for an additional day. The crucibles were then removed from the electric furnace and quenched to room temperature. A 1.3 N $HNO_3$ aqueous solution followed by rinsing in distilled water was used to clean the material of soluble unreacted compounds.

**Other orthophosphate synthesis methods**

A process for synthesizing monazite ceramics that contain a variety of cations (including both thorium and uranium) has been described by McCarthy et al. (1978). This synthesis employed nitrate solutions of the REs, calcium, thorium, $UO_2$, $NH_4H_2(PO_4)$, and colloidal $SiO_2$ that were initially heated to form a paste. The paste was subsequently calcined at 600°C for two hours. The resulting material was ground and cold-pressed into pellets that were fired in the range 1050 to 1200°C for four or 48 hours. Different charge-compensation mechanisms that involve the addition of calcium or silicon were investigated. In the case of the highest concentrations of uranium, phase-pure monazite was not obtained, and the phases $U_3(PO_4)_4$ and $U_3P_2O_{10}$ were observed along with the dominant monazite component.

A direct precipitation technique for the preparation of the RE orthophosphates has been described by Hikichi et al. (1978) in which a 0.05 mol/l solution of the rare-earth trichloride was added to a dilute, stirred $H_3(PO_4)$ solution. The mixed solutions were then maintained at 20, 50, and 90°C for 1 to 900 days and were titrated to maintain a constant pH by adding $H_3(PO_4)$ or other phosphates. Both the hydrated low-temperature hexagonal forms of the rare-earth phosphates (as discussed in the previous section on Chemical composition) and the anhydrous RE orthophosphates were produced by Hikichi et al. (1978).

Hydrothermal methods have been used by Gratz and Heinrich (1997) to synthesize solid solutions of $(Ce,Y)PO_4$ at temperatures in the range of 300 to 1000°C and at pressures between two and 15 kbar. These workers reported the formation of two immiscible phases (monazite and xenotime) over a wide range of compositions. Complete

solid solutions between $La(PO_4)$ and $(Ca_{0.5}Th_{0.5})PO_4$ were also hydrothermally synthesized at 780°C and 200 MPa by Podor and Cuney (1997). Their results show: (1) that the substitution of thorium in monazite is not limited by the temperature and pressure conditions experienced by granitic magmas, and (2) that radiogenic lead is stable in natural monazites.

## APPLICATIONS OF RE-, SC -, AND Y-ORTHOPHOSPHATES

### Orthophosphate waste forms for actinides and high-level radioactive wastes

The application of the RE orthophosphates to the disposal or long-term storage of actinides and high-level radioactive wastes is thoroughly treated by Ewing and Wang in this volume. This concept was advanced by Boatner et al. (1980, 1981a, 1983) and McCarthy et al. (1978), and the use of monazite as a radioactive waste form was subsequently reviewed by Boatner and Sales (1988). In brief, this concept was initially based on four known and established primary characteristics of monazite that are clearly advantageous for its use as a radioactive waste form. These characteristics are:

(1) The established chemical stability of monazite in the earth's crust over geological time scales (Floran et al. 1981b, Pasteels 1970).

(2) The ability of monazite to incorporate large amounts of thorium and uranium (see Table 1) and the structural compatibility of monazite with $Pu(PO_4)$ (Bamberger et al. 1984).

(3) The ability of monazite to recover from displacive radiation damage and thereby retain its crystallinity and chemical integrity [Ewing and Wang, this volume; Meldrum et al. (1997a,b,c; 1998, 2000)].

(4) Monazite exhibits a negative temperature coefficient of solubility and, therefore, will actually be less soluble during the highly radioactive early "thermal" period of a high-level radioactive waste form (Marinova and Yaglov 1976).

In the case of the disposal of high-level light water reactor waste, these wastes intrinsically contain up to 35 wt % rare-earth oxides that could be directly converted to form part of the monazite host matrix. Because Ewing and Wang (this volume) have provided a comparison of the properties of monazite-based waste forms to those of other crystalline host media and nuclear waste phosphate glasses, no further details regarding this application of the rare-earth orthophosphates will be given here.

### Gamma- and X-ray scintillator and phosphor applications

The heavy zircon-structure rare-earth orthophosphate $Lu(PO_4)$ (or LOP), when activated with cerium, has been found to be a fast, efficient, and dense scintillator for the detection of gamma rays (Lempicki et al. 1993, Wojtowicz et al. 1994, 1995; Moses et al. 1997, 1998). This scintillator was found to have a 24 nsec decay time constant and a light output that is over double that of bismuth germanium oxide. Another Lu-based, but non-phosphate efficient and fast scintillator, $Lu_2O(SiO_4)$:Ce (or LSO) is currently finding widespread application in medical diagnostic equipment such as positron emission tomography systems. This lutetium silicate has a very important advantage over LOP in that the compound melts congruently, and large single crystals can be extracted from the melt (i.e., Czochralski growth). As previously noted, top-seeded-solution or hydrothermal techniques will have to be developed in order to grow large single crystals of LOP, and this has yet to be accomplished. More recently, Nd-activated $Lu(PO_4)$ and $Y(PO_4)$ have been found to be interesting VUV scintillators whose short wavelength output (~190 nm) can be matched to appropriately activated proportional counters, thereby eliminating the need for photomultiplier tubes and their associated electronics (Wisniewski et al. 2002a,b). Other candidate orthophosphate scintillators and phosphors

have been identified by Moses et al. (1997, 1998). Specifically, Eu- and Sm-doped $Lu(PO_4)$, $Sc(PO_4)$, and $Y(PO_4)$ were found to have a high light output in the wavelength range of 600 to 900 nm. In the case of $Lu(PO_4)$:20%Eu, Moses et al. reported a value of 123,171 photons per MeV in the 600-900 nm range. This light-output region matches the high quantum efficiency region of silicon photodiode detectors. Orthophosphates doped with Tb, Dy, Er, Pr, and Tm were also reported by Moses et al. to have a significant light output when excited by x-rays. Although the decay times of some of these scintillators may be too long for them to find applications in some medical imaging devices, they may be appropriate for other applications, including imaging screens and displays.

Allison et al. (1995) have shown that $Lu(PO_4)$:(1% Dy, 2% Eu) can be used as a thermophosphor that can be calibrated to carry out high-temperature measurements on moving parts in a remote, non-contact mode. Similarly, both $Y(PO_4)$ and $Sc(PO_4)$ doped with Dy and Eu can be used for remote, non-contact, high-temperature measurements, e.g., on pistons operating in a reciprocating engine, on moving turbine blades, or in environments where it is not practical to use metallic thermocouples - such as in microwave sintering furnaces (Allison et al. 1998, 1999).

**Orthophosphates as weak interfaces in ceramic composites**

Morgan and Marshall (1993, 1995, 1996, 1997) and Marshall et al. (1997, 1998) have introduced the concept of using $La(PO_4)$, xenotime, and other rare-earth orthophosphates as weak interfaces in ceramic composites. In this concept, the fiber component of a ceramic composite is coated with a material (e.g., a rare-earth orthophosphate) that will debond from the fiber. This allows fiber slippage or "pull out" to occur as a mechanism for arresting crack propagation by deflecting the crack along the interface, thereby avoiding failure by brittle fracture. The demands on a coating material of this type are severe. Morgan and Marshall (1995) have identified the following required characteristics for a weak-interface material: (1) chemical and morphological compatibility, (2) refractory behavior, (3) stability in oxidizing (and limited reducing) conditions, (4) stability in $H_2O$ vapor and $CO_2$ environments, and (5) weak interfaces that exhibit the desired debonding behavior.

The application of weak-interface RE and Y orthophosphate coatings to both $Al_2O_3$ fibers and $ZrO_2$-based ceramics has been investigated. Marshall et al. (1997) have studied composites formed by alternating layers of monazite and various types of $ZrO_2$ (e.g., Y-$ZrO_2$ and Ce-$ZrO_2$). They found that no reaction occurred between $La(PO_4)$ and Y-$ZrO_2$ at temperatures as high as 1600°C. Similar results were obtained by Marshall et al. (1998) for the case of the $Al_2O_3/La(PO_4)$ system, and as long as the ratio of lanthanum to phosphorous was near 1:1, the $La(PO_4)/Al_2O_3$ interface remained sufficiently weak to exhibit debonding and deflect cracks. Reactions occurred, however, if excess La or P was present, and other phases [e.g. berlinite, $Al(PO_4)$] were formed on heating to 1600°C. Research on structural ceramic applications of this type is continuing at several laboratories, and clearly, the development of applications of this nature would create a significantly increased demand for the rare-earth elements.

**Other applications of RE-, Sc -, and Y-orthophosphates**

The rare-earth orthophosphates plus $Y(PO_4)$ and $Sc(PO_4)$ represent the basis for a set of reference samples for rare-earth analysis, developed by Jarosewich and Boatner (1991). The sixteen orthophosphates that are included in this microprobe reference sample set were initially synthesized in single-crystal form by using the high-temperature-solvent process described in a previous section this chapter. High-purity oxides and unused Pt growth crucibles were utilized in all of the single-crystal growth operations. These orthophosphates were determined to be homogeneous on a micron

scale, and they were found to be stable under exposure to an electron beam for extended periods of time. In terms of contamination from other REs, neutron activation analysis revealed only traces of RE elements other than the principal $RE(PO_4)$ component. As discussed previously, Donovan et al. (2002a,b) have recently re-examined these reference samples in terms of potential lead contamination arising from the use of the lead pyrophosphate flux in the crystal growth process. These microprobe analytical reference materials are now widely distributed on an international scale, and they have proven to be useful for the rare-earth analysis of minerals and a wide range of other materials.

The heavier rare-earth phosphates are excellent hosts for the incorporation of other rare-earth dopants, and accordingly, host systems such as $Lu(PO_4)$ have been used in investigations of new materials for potential applications as micro lasers (Rapaport et al. 1999a,b). The lasing properties of crystals of $Lu(PO_4)$ doped with Nd were studied by Rapaport et al. (1999a), who reported that 88% of the pump power (at 804.4 nm) was absorbed in a 1.0 mm-thick crystal. The $Lu(PO_4)$:Er system has also been investigated by Rapaport et al. (1999b), but the prospects for using this system as a laser were not encouraging because of the difficulty in achieving a population inversion as a result of a low absorption of the 804 nm pump wavelength and up-conversion effects that serve to deplete the population of the upper Er level.

## STRUCTURAL PROPERTIES OF RE-, SC-, AND Y-ORTHOPHOSPHATES

### Early crystallographic studies

The structural properties of the rare-earth and related orthophosphates have been treated for over 60 years with varying degrees of detail and increasing levels of sophistication by several workers—beginning, it appears, with the work of Parish (1939) and Gliszczynski (1939). Structural information was obtained on $La(PO_4)$, $Ce(PO_4)$, $Pr(PO_4)$, and $Nd(PO_4)$ by Rose Mooney in 1944 at the Metallurgical Laboratory of the University of Chicago in conjunction with the Manhattan Project, and the results were later published in the open literature (Mooney 1948). The structural results for the hexagonal form of $Ce(PO_4)$ and related phosphates were described in more detail in a later publication (Mooney 1950). The relationship between the ionic radii and the structures of RE phosphates, vanadates, and arsenates was examined by Carron et al. (1958). Unit cell data for the monazite-type RE orthophosphates [including data for $PmPO_4$)] were determined by Weigel et al. (1965), and data for the zircon-type rare-earth phosphates, including $Sc(PO_4)$, and for several rare-earth arsenates and vanadates were obtained by Schwarz (1963). Crystallographic data have been obtained by Kizilyalli and Welch (1976), who prepared crystalline powders by means of a direct precipitation and calcining technique and by Pepin and Vance (1981) who also prepared and investigated a series of precipitated rare-earth orthophosphate powders. The crystal structure of natural monazite was studied by Ueda (1967) using a sample from Ishikawa-yama, Fukushima Pref. in Japan, and refinements of the structure of heat-treated monazite from India have been carried out by Ghouse (1968), whose results were described previously in the section on radiation damage effects.

### Crystal chemical background and characteristics

The anhydrous 4*f* transition-series (rare-earth) elements undergo a change in ionic radius in accordance with the well-known lanthanide contraction, in which the lanthanide ions exhibit a decreasing ionic radius as the atomic number increases. This change in ionic radius is accompanied by a change in the RE orthophosphate crystal structure as one goes across the series from the light end member $La(PO_4)$ to the heavy end-member $Lu(PO_4)$. The orthophosphates from $La(PO_4)$ to $Eu(PO_4)$ only exist in the monoclinic monazite structure, space group $P2_1/n$, $Z = 4$, whereas the orthophosphates from Ho to Lu are only

found with the tetragonal zircon structure, space group $I4_1/amd$, $Z = 4$. The orthophosphates $Gd(PO_4)$, $Tb(PO_4)$, and $Dy(PO_4)$ have been synthesized in both the monoclinic and tetragonal forms (Ushakov et al. 2001, Bondar et al. 1976) with the tetragonal structure representing the high-temperature structural form. Xenotime, $Y(PO_4)$, and pretulite, $Sc(PO_4)$, have the tetragonal zircon structure. These two different orthophosphate structural types are also common to most of the rare-earth vanadates and arsenates. The xenotime structure, however, only accepts the larger rare-earth ions as the metal-oxide tetrahedra increase in size in going from $PO_4$ to $AsO_4$ to $VO_4$. Ushakov et al. (2001) have noted that in the rare-earth vanadate series, only $La(VO_4)$ exhibits the monoclinic monazite structure—although the vanadates from Ce to Nd have been reported to have a low-temperature monazite polymorph. These workers also noted that, in the case of the actinide-series elements, $Am(VO_4)$ has the tetragonal zircon structure, whereas $Pu(PO_4)$ and $Am(PO_4)$ exhibit the monoclinic monazite structure. In the case of the orthosilicates, either the tetragonal structure of $Th(SiO_4)$ (thorite) or the monoclinic monazite structure (huttonite) can be formed – depending on the formation temperature—with the tetragonal zircon structural form being stable at higher temperatures. An extremely useful compilation that illustrates the structural relationships between the phosphates, silicates, arsenates, and vanadates of the rare earths and some actinides is shown in Figure 7 (after Ushakov et al. 2001).

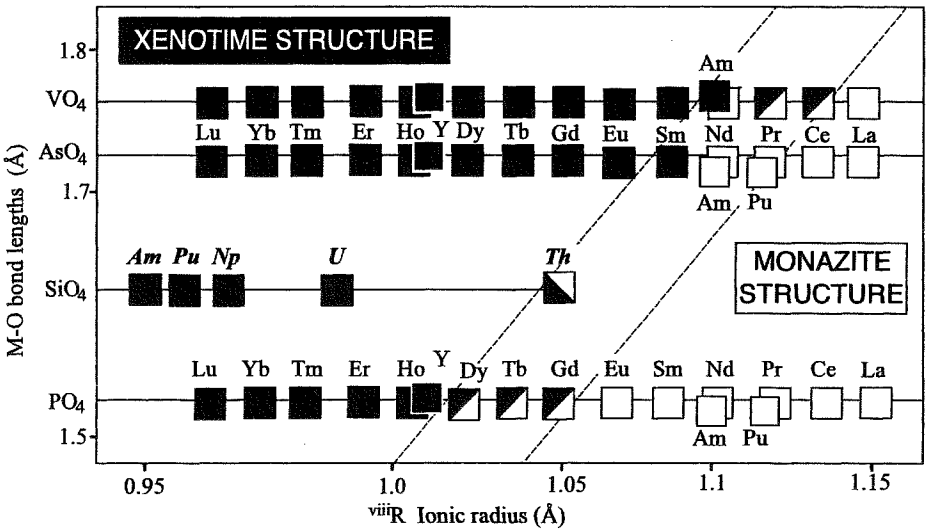


**Figure 7.** Illustration of the relationship between phosphates, vanadates, arsenates and silicates with the xenotime or monazite structure for compounds of the type $R(MO_4)$. Here, R represents: $RE^{3+}$, $An^{3+}$; $An^{4+}$; and M represents P, Si, As, or V. After Ushakov et al. (2001).

A major distinguishing crystal-chemical feature between the monoclinic monazite-structure compounds and those with the tetragonal zircon or xenotime structure lies in the oxygen coordination of the rare-earth ion in the RE-oxygen polyhedra. In the monazite structure, the RE ion is coordinated with nine oxygen ions—one of which, however, has a somewhat longer bond length (2.78 Å) than the others (~2.53 Å). A view of the $REO_9$ polyhedron with one attached $PO_4$ tetrahedron is offered in Figure 8 (Beall et al. 1981). In the tetragonal zircon structure, the RE, Y, or Sc ions are coordinated with 8 surrounding oxygen ions, and this type of coordination is illustrated in Figure 9 (Milligan et al. 1982).

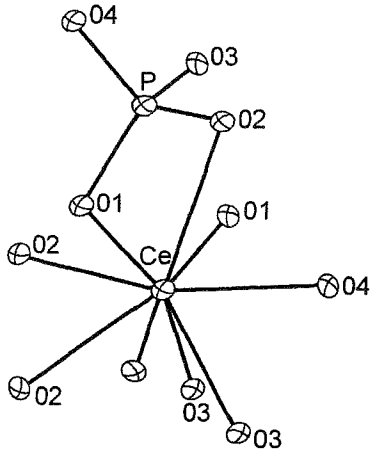


**Figure 8.** The nature of the nine-fold coordination characteristic of the monoclinic monazite-structure ($P2_1/n$) orthophosphates is illustrated in a view of $Ce(PO_4)$ that also shows the linkage to one of the surrounding $PO_4$ structural units (after Beall et al. 1981).

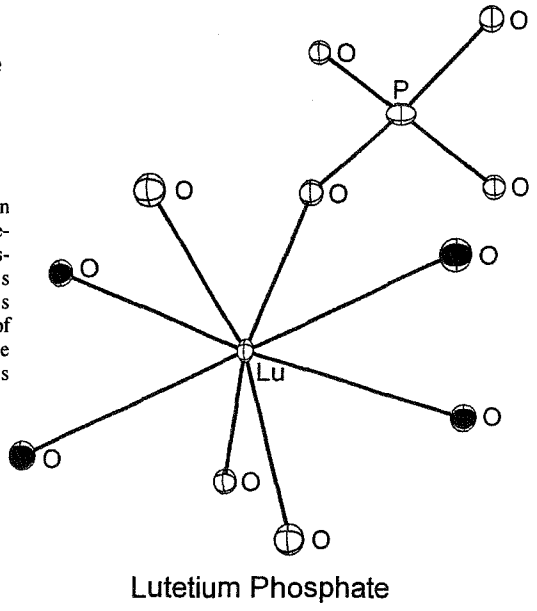


**Figure 9.** The eight-fold coordination characteristic of the tetragonal, xenotime-structure heavy rare-earth orthophosphates and of $Y(PO_4)$ and $Sc(PO_4)$ is shown. The bond lengths in this structure are equivalent in two sets of four identical-length bonds. The linkage to one of the surrounding $PO_4$ units is also shown (after Milligan et al. 1982).

The application of monoclinic monazites to the chemical sequestration of radioactive wastes has been noted in a prior section of the present chapter, and it is reviewed in detail by Ewing and Wang (this volume). From the crystal-chemical point of view, it has been previously suggested (Beall et al. 1981) that the observed ability of monazites to incorporate the diverse set of cations found in most radioactive wastes may be due to a relaxation of chemical constraints associated with the irregular 9-fold coordination.

**Single-crystal monazite and xenotime structural refinements**

Single crystals of the anhydrous monazite and xenotime structure RE orthophosphates plus $Y(PO_4)$ and $Sc(PO_4)$ that were grown by the $Pb_2P_2O_7$ flux technique described previously have been used in carrying out a series of single-crystal structural refinements by various workers. The structure of $La(PO_4)$ was determined by Mullica et al. (1984) and that of $Ce(PO_4)$ by Beall et al. (1981). Structural refinements of $Pr(PO_4)$ and $Nd(PO_4)$ were reported by Mullica et al. (1985a), of $Sm(PO_4)$, $Eu(PO_4)$, and $Gd(PO_4)$ by Mullica et al. (1985b), of $Tb(PO_4)$, $Dy(PO_4)$ and $Ho(PO_4)$ by Milligan et al.

(1983a), and the structures of $Er(PO_4)$, $Tm(PO_4)$, and $Yb(PO_4)$ by Milligan et al. (1983b). The structure of synthetic xenotime, pretulite and the RE series end member $Lu(PO_4)$ were described by Milligan et al. (1982). The structure of the mixed RE/actinide crystal $Ce_{0.9}U_{0.1}(PO_4)$ was refined and reported by Mullica et al. (1989). More recently the same suite of synthetic flux-grown orthophosphate single crystals [with the exception of $Sc(PO_4)$] was re-examined, and the crystal chemistry of these materials was described by Ni et al. (1995). These latter workers also carried out refinements for natural monazite and natural xenotime samples. The crystal data and the results of the single-crystal structural refinements based on the recent work of Ni et al. (1995) are shown in Table 3 for the monazite-structure materials and in Table 4 for the xenotime-structure phases. The data for $Sc(PO_4)$ and the available structural data for $Pm(PO_4)$ are given in Table 5.

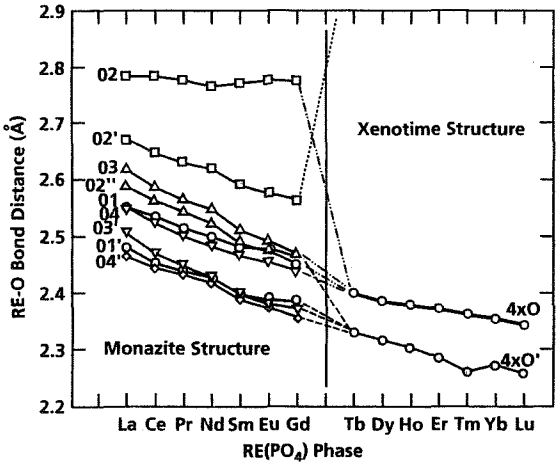


**Figure 10.** The variation of the rare-earth-to-oxygen bond distances are shown for a number of rare-earth orthophosphate compounds with the monoclinic monazite (nine-fold oxygen coordinated) and tetragonal xenotime (eight-fold oxygen coordinated) structures (after Ni et al. 1995).

For the monoclinic structure, there are nine distinct bond distances between the RE and oxygen ions (versus two sets of four equivalent distances for the xenotime structures). The RE-oxygen bond distances have been plotted for the various monazite and xenotime structure RE phases by Ni et al. (1995), and their results are shown in Figure 10. These workers point out the regular variation of the RE cation-to-oxygen bond distances that is typical of both the monazite and xenotime structures. The nine-fold geometric coordination of the light RE, monoclinic orthophosphates and a view of the resulting coordination between the RE ions and the orientation of the surrounding $PO_4$ tetrahedra is shown in Figure 11. This figure represents a view that is slightly tilted from looking directly along the *c* axis of the structure. The single-crystal refinement data were carefully examined by Mullica et al. (1984) for the case of $La(PO_4)$, and these workers determined that the proper description of this system was that of a pentagonal interpenetrating tetrahedral polyhedron (PITP). Figure 12(a) shows a typical $La(PO_4)$ structural unit that is reoriented in Figure 12(b) to illustrate the PITP polyhedron and the $C_s$ symmetry plane. Figure 12(c) illustrates the idealized PITP and $C_s$ plane of symmetry. The bidentate bonding to two of the $PO_4$ tetrahedra is illustrated in Figure 13 (top), and Figure 13 (bottom) shows a view illustrating the pentagonal arrangement of the RE-O bonds to the five $PO_4$ tetrahedral units that lie in the pentagonal plane.

TABLE 3. Crystal data and results of structure refinements for monazite structure phases

| Phases | Monazite* | $La(PO_4)$ | $Ce(PO_4)$ | $Pr(PO_4)$ | $Nd(PO_4)$ | $Sm(PO_4)$ | $Eu(PO_4)$ | $Gd(PO_4)$ |
|---|---|---|---|---|---|---|---|---|
| **Unit cells by least squares (unconstrained)** | | | | | | | | |
| $a$ (Å) | 6.7902(10) | 6.8313(10) | 6.7880(10) | 6.7596(8) | 6.7352(10) | 6.6818(12) | 6.6613(10) | 6.6435(9) |
| $b$ (Å) | 7.0203(6) | 7.0705(9) | 7.0163(8) | 6.9812(10) | 6.9500(9) | 6.8877(9) | 6.8618(9) | 6.8414(10) |
| $c$ (Å) | 6.4674(7) | 6.5034(9) | 6.4650(7) | 6.4344(9) | 6.4049(8) | 6.3653(9) | 6.3491(8) | 6.3281(6) |
| $\alpha$ (°) | 90.007(8) | 89.993(11) | 89.997(9) | 89.997(11) | 90.004(10) | 89.982(11) | 90.005(11) | 90.013(9) |
| $\beta$ (°) | 103.38(1) | 103.27(1) | 103.43(1) | 103.53(1) | 103.68(1) | 103.86(1) | 103.96(1) | 103.976(9) |
| $\gamma$ (°) | 89.989(9) | 89.981(11) | 90.011(10) | 89.979(10) | 89.967(11) | 89.979(12) | 89.975(12) | 89.983(11) |
| No. collected | 3541 | 1945 | 1910 | 1884 | 1860 | 1812 | 1797 | 1778 |
| No. unique | 945 | 891 | 943 | 861 | 851 | 827 | 819 | 811 |
| No. > $3\sigma_I$ | 774 | 790 | 717 | 753 | 763 | 732 | 712 | 710 |
| $R_{merge}$ | 0.012 | 0.014 | 0.011 | 0.012 | 0.010 | 0.013 | 0.012 | 0.011 |
| $R$ | 0.015 | 0.017 | 0.014 | 0.016 | 0.015 | 0.016 | 0.016 | 0.016 |
| $R_w$ | 0.023 | 0.026 | 0.019 | 0.021 | 0.017 | 0.019 | 0.019 | 0.019 |
| **Largest peaks on difference maps (e/Å³)** | | | | | | | | |
| (+) | 0.741 | 0.897 | 0.653 | 0.971 | 0.841 | 0.885 | 1.039 | 1.073 |
| (−) | 0.704 | 1.023 | 0.632 | 1.276 | 0.995 | 1.236 | 0.884 | 1.265 |
| **Atomic positions** | | | | | | | | |
| RE $x$ | 0.28152(4) | 0.28154(2) | 0.28182(2) | 0.28177(2) | 0.28178(3) | 0.28153(3) | 0.28152(3) | 0.28150(3) |
| $y$ | 0.15929(4) | 0.16033(2) | 0.15914(2) | 0.15862(3) | 0.15806(3) | 0.15638(3) | 0.15595(3) | 0.15529(3) |
| $z$ | 0.10006(4) | 0.10068(2) | 0.10008(2) | 0.09988(2) | 0.09950(3) | 0.09813(3) | 0.09757(3) | 0.09695(3) |
| $B$ (Å²) | 0.329(4) | 0.294(3) | 0.431(3) | 0.351(3) | 0.280(3) | 0.228(3) | 0.193(3) | 0.306(3) |
| P $x$ | 0.3048(2) | 0.3047(1) | 0.3047(1) | 0.3040(1) | 0.3037(1) | 0.3034(2) | 0.3029(1) | 0.3031(2) |
| $y$ | 0.1630(2) | 0.1639(1) | 0.1635(1) | 0.1630(1) | 0.1626(1) | 0.1618(2) | 0.1615(1) | 0.1612(2) |
| $z$ | 0.6121(2) | 0.6121(1) | 0.6124(1) | 0.6127(1) | 0.6127(1) | 0.6130(2) | 0.6130(1) | 0.6131(2) |
| $B$ (Å²) | 0.31(2) | 0.33(1) | 0.51(1) | 0.36(1) | 0.30(1) | 0.25(2) | 0.24(1) | 0.38(2) |
| O1 $x$ | 0.2501(5) | 0.2503(4) | 0.2508(4) | 0.2498(4) | 0.2502(4) | 0.2499(5) | 0.2513(4) | 0.2539(5) |
| $y$ | 0.0068(5) | 0.0077(4) | 0.0055(4) | 0.0051(4) | 0.0046(4) | 0.0020(5) | 0.0012(4) | 0.0013(5) |
| $z$ | 0.4450(5) | 0.4477(4) | 0.4458(4) | 0.4441(4) | 0.4430(4) | 0.4405(5) | 0.4409(4) | 0.4385(5) |
| $B$ (Å²) | 0.63(6) | 0.78(4) | 0.93(4) | 0.69(4) | 0.67(5) | 0.57(6) | 0.68(5) | 0.80(6) |
| O2 $x$ | 0.3814(5) | 0.3799(4) | 0.3811(4) | 0.3816(4) | 0.3815(4) | 0.3822(5) | 0.3833(4) | 0.3837(5) |
| $y$ | 0.3307(6) | 0.3315(3) | 0.3320(3) | 0.3327(4) | 0.3331(4) | 0.3341(5) | 0.3350(4) | 0.3346(5) |
| $z$ | 0.4975(6) | 0.4964(4) | 0.4982(4) | 0.4990(4) | 0.4987(4) | 0.5008(5) | 0.5017(4) | 0.5024(5) |
| $B$ (Å²) | 0.69(6) | 0.61(4) | 0.80(4) | 0.67(4) | 0.61(4) | 0.57(5) | 0.52(5) | 0.66(5) |
| O3 $x$ | 0.4742(6) | 0.4748(4) | 0.4745(4) | 0.4744(4) | 0.4747(4) | 0.4748(5) | 0.4743(4) | 0.4729(5) |
| $y$ | 0.1070(6) | 0.1071(4) | 0.1054(4) | 0.1046(4) | 0.1040(4) | 0.1025(5) | 0.1022(4) | 0.1016(5) |
| $z$ | 0.8037(6) | 0.8018(4) | 0.8042(4) | 0.8057(4) | 0.8073(4) | 0.8102(5) | 0.8116(4) | 0.8126(5) |
| $B$ (Å²) | 0.73(6) | 0.63(4) | 0.84(4) | 0.63(4) | 0.62(5) | 0.56(5) | 0.53(5) | 0.62(5) |
| O4 $x$ | 0.1274(5) | 0.1277(3) | 0.1268(3) | 0.1260(4) | 0.1249(4) | 0.1217(5) | 0.1204(4) | 0.1187(5) |
| $y$ | 0.2153(5) | 0.2168(3) | 0.2164(4) | 0.2150(4) | 0.2153(4) | 0.2125(5) | 0.2135(4) | 0.2138(5) |
| $z$ | 0.7104(6) | 0.7101(4) | 0.7108(4) | 0.7120(4) | 0.7127(4) | 0.7113(5) | 0.7119(5) | 0.7131(5) |
| $B$ (Å²) | 0.63(6) | 0.66(4) | 0.77(4) | 0.62(4) | 0.52(4) | 0.57(5) | 0.48(4) | 0.67(5) |

* Natural sample.

**TABLE 4.** Crystal data and results of structure refinements for xenotime structure phases

| Phases | Xenotime* | $Tb(PO_4)$ | $Dy(PO_4)$ | $Ho(PO_4)$ | $Er(PO_4)$ | $Tm(PO_4)$ | $Yb(PO_4)$ | $Lu(PO_4)$ |
|---|---|---|---|---|---|---|---|---|
| | | | | **Unit cells by least squares (unconstrained)** | | | | |
| $a$ (Å) | 6.8951(6) | 6.9319(12) | 6.9046(12) | 6.8772(8) | 6.8510(13) | 6.8297(7) | 6.8083(9) | 6.7848(14) |
| $b$ (Å) | 6.8943(5) | 6.9299(11) | 6.9057(9) | 6.8773(12) | 6.8505(16) | 6.8290(10) | 6.8103(6) | 6.7807(10) |
| $c$ (Å) | 6.0276(6) | 6.0606(11) | 6.0384(6) | 6.0176(8) | 5.9968(10) | 5.9798(10) | 5.9639(5) | 5.9467(6) |
| $\alpha$ (°) | 89.993(7) | 90.016(14) | 90.013(9) | 90.004(13) | 89.986(16) | 90.009(12) | 89.987(7) | 89.969(10) |
| $\beta$ (°) | 90.012(8) | 89.997(14) | 90.019(12) | 89.991(10) | 89.963(14) | 89.967(11) | 89.997(9) | 90.008(12) |
| $\gamma$ (°) | 90.018(7) | 89.997(13) | 90.006(13) | 89.988(13) | 90.026(17) | 89.996(10) | 90.019(9) | 90.010(14) |
| No. collected | 919 | 924 | 922 | 903 | 891 | 884 | 890 | 1046 |
| No. unique | 145 | 135 | 134 | 132 | 130 | 129 | 128 | 151 |
| No. > $3\sigma_I$ | 109 | 113 | 112 | 111 | 108 | 107 | 97 | 119 |
| $R_{merge}$ | 0.018 | 0.010 | 0.011 | 0.014 | 0.014 | 0.020 | 0.013 | 0.016 |
| $R$ | 0.016 | 0.009 | 0.008 | 0.015 | 0.012 | 0.017 | 0.013 | 0.009 |
| $R_w$ | 0.028 | 0.019 | 0.019 | 0.021 | 0.022 | 0.026 | 0.033 | 0.012 |
| | | | | **Largest peaks on difference maps (e/Å³)** | | | | |
| (+) | 0.624 | 0.464 | 0.496 | 0.669 | 1.105 | 0.934 | 0.817 | 0.978 |
| (−) | 0.766 | 0.498 | 0.537 | 1.283 | 0.922 | 1.187 | 0.734 | 0.802 |
| | | | | **Atomic positions** | | | | |
| RE $x$ | 0 | 0 | 0 | 0 | 0 | 0 | 0 | 0 |
| $y$ | 0.75 | 0.75 | 0.75 | 0.75 | 0.75 | 0.75 | 0.75 | 0.75 |
| $z$ | 0.125 | 0.125 | 0.125 | 0.125 | 0.125 | 0.125 | 0.125 | 0.125 |
| $B$ (Å²) | 0.455(7) | 0.350(4) | 0.346(4) | 0.049(6) | 0.406(7) | 0.104(7) | 0.28(1) | 0.245(2) |
| P $x$ | 0 | 0 | 0 | 0 | 0 | 0 | 0 | 0 |
| $y$ | 0.25 | 0.25 | 0.25 | 0.25 | 0.25 | 0.25 | 0.25 | 0.25 |
| $z$ | 0.375 | 0.375 | 0.375 | 0.375 | 0.375 | 0.375 | 0.375 | 0.375 |
| $B$ (Å²) | 0.62(2) | 0.43(2) | 0.43(2) | 0.26(4) | 0.48(4) | 0.14(4) | 0.50(7) | 0.31(2) |
| O $x$ | 0 | 0 | 0 | 0 | 0 | 0 | 0 | 0 |
| $y$ | 0.0753(6) | 0.0764(5) | 0.0760(6) | 0.0757(8) | 0.0743(9) | 0.072(1) | 0.074(1) | 0.0735(4) |
| $z$ | 0.2158(6) | 0.2175(5) | 0.2162(6) | 0.2165(8) | 0.216(1) | 0.213(1) | 0.215(1) | 0.2138(4) |
| $B$ (Å²) | 0.94(6) | 0.60(5) | 0.61(5) | 0.38(8) | 0.65(9) | 0.3(1) | 0.5(1) | 0.52(4) |

* Natural sample.

**Table 5.** $Sc(PO_4)$ (pretulite) and $Pm(PO_4)$ crystallographic data.

| *Summary data* | | | *$ScPO_4$ bond and contact distances (Å) & bond angles (°)* | |
|---|---|---|---|---|
| | *$ScPO_4$* | *$PmPO_4$* | | |
| *a* (Å) | 6.574(1) | 6.72 | M-O | 2.153(1) |
| *b* (Å) | - | 6.89 | | 2.260(1) |
| *c* (Å) | 5.791(1) | 6.37 | Avg. | 2.206 |
| β | - | 104° 17′ | P-O | 1.534(1) |
| $D_c$ (g $cm^{-3}$) | 3.71 | 5.62 | **Phosphate Group** | |
| V ($Å^3$) | 250.27 | - | O(1)-O(2) O(3)-O(4) | 2.374(3) |
| | | | O(1)-O(3), O(4) O(2)-O(3), O(4) | 2.569(2) |
| | | | O(1)-P-O(2) O(3)-P-O(4) | 101.39(2) |
| | | | O(1)-P-O(3), O(4) O(2)-P-O(3), O(4) | 113.72(2) |
| | | | Avg. (O-P-O) | 109.61 |

$Sc(PO_4)$ data after Milligan et al. (1982); $Pm(PO_4)$ data after Kizilyalli & Welch (1976)

***$ScPO_4$ atomic positions and thermal parameters (Å × $10^2$)[a]***

| *Atom* | *x* | *y* | *z* | $U_1$ | $U_{22}$ | $U_{33}$ | $U_1$ | $U_{13}$ | $U_{23}$ |
|---|---|---|---|---|---|---|---|---|---|
| Sc | 0 | 3/4 | 1/8 | 0.43(1) | - | 0.34(2) | 0 | 0 | 0 |
| P | 0 | 1/4 | 3/8 | 0.39(2) | - | 0.24(3) | 0 | 0 | 0 |
| O | 0 | 0.4305(2) | 0.2071(2) | 0.89(5) | 0.52(4) | 0.38(3) | 0 | 0 | 0.07(3) |

[a] The anisotropic temperature factors are of the form:
$T = \exp[-2\pi^2(U_{11}h^2a^{*2}+U_{22}k^2b^{*2}+U_{33}l^2c^{*2}+2U_{12}hka^*b^*\cos\gamma^*+2U_{13}hla^*c^*\cos\beta^*+2U_{23}klb^*c^*\cos\alpha^*)]$
where $U_{ij}$ values are the thermal parameters denoted in terms of mean-squared amplitudes of vibration.

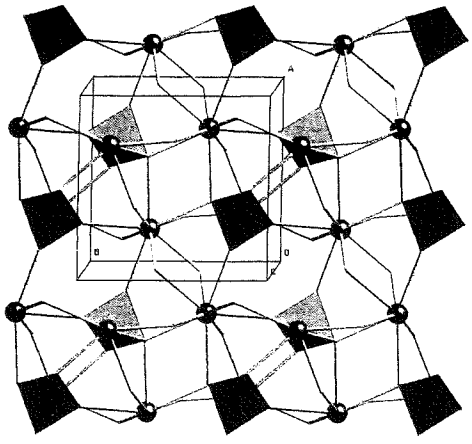

**Figure 11.** The nine-fold coordination of the rare-earth ion in the monoclinic monazite structure is illustrated along with the linkage to various surrounding $PO_4$ tetrahedral units. This view is slightly off of "looking down" the *c*-axis of the structure.

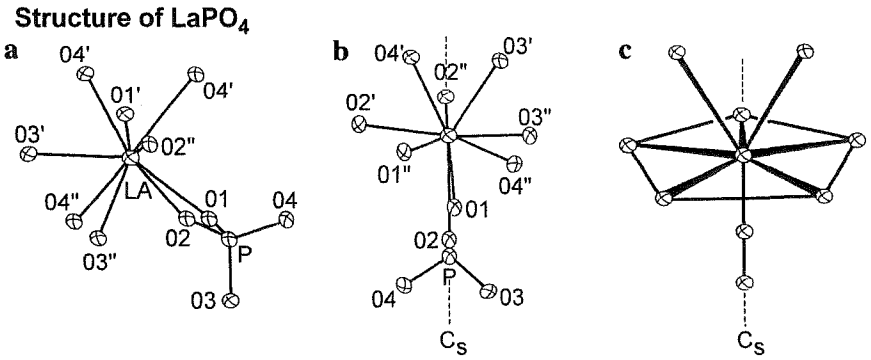


**Figure 12.** (a) Randomly oriented nine-fold coordinated unit of $La(PO_4)$ with one attached $PO_4$ tetrahedron, (b) the same structural unit as shown in (a) but reoriented to the reveal thecoordination described in the text and the $C_s$ symmetry plane, (c) idealized pentagonal rare-earth-to-oxygen bond arrangement (after Mullica et al. 1984).

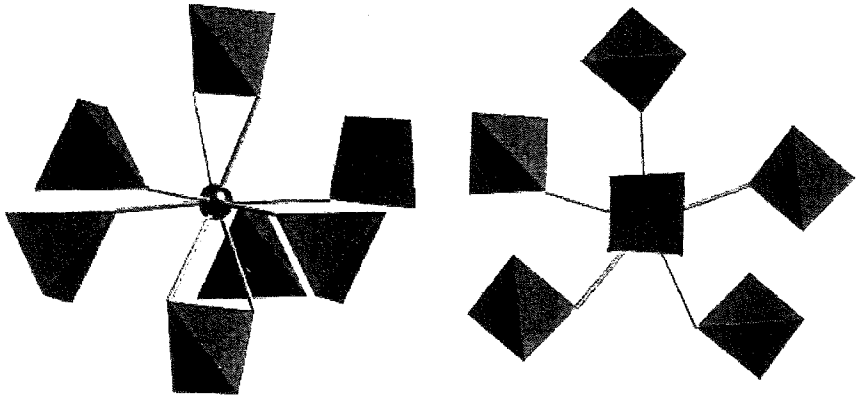

**Figure 13.** (Left) The bidentate bonding to two of the $PO_4$ tetrahedral units in the monoclinic monazite structure is illustrated. (Right) The pentagonal arrangement of the rare-earth-to-oxygen bonds on five surrounding $PO_4$ tetrahedra is illustrated in a projected view.

The structure of the monoclinic materials consists of chain-like interlocked strands of nine-fold coordinated polyhedra that are linked together by the $PO_4$ tetrahedral units (Mullica et al. 1985a,b), sometimes referred to as "polyhedron-tetrahedron" chains (Ni et al. 1995). An apical linking of the light rare-earth atoms by the distorted tetrahedral groups forms the chain-like monoclinic monazite structure. A stereoscopic view of the interlocking mechanism of the chain-like units for the case of the monoclinic RE orthophosphate structure is shown in Figure 14 (Mullica et al. 1985a,b).

In the xenotime structure, there are two sets of four equivalent bond distances (Ni et al. 1995). This coordination is illustrated in Figure 15 (left; after Milligan et al. 1982). These two sets of four equivalent bond distances are oriented orthogonal to each other, forming two unique and orthogonal interpenetrating tetrahedra. This results in a RE-O configuration (Fig. 15, right) that has been described by Milligan et al. (1983c) as a distorted dodecahedron $D_{2d}$ (bibisphenoid) derived from a distorted cube. The relationship between the eight-fold-coordinated RE ion and the surrounding $PO_4$ tetrahedral units is illustrated in Figure 16. This figure shows the details of the molecular packing in the unit cell of the tetragonal RE orthophosphate structure in a stereo view and clearly illustrates how the RE-$PO_4$ polyhedral units fit together. Ni et al. (1995) pointed out that the RE-P

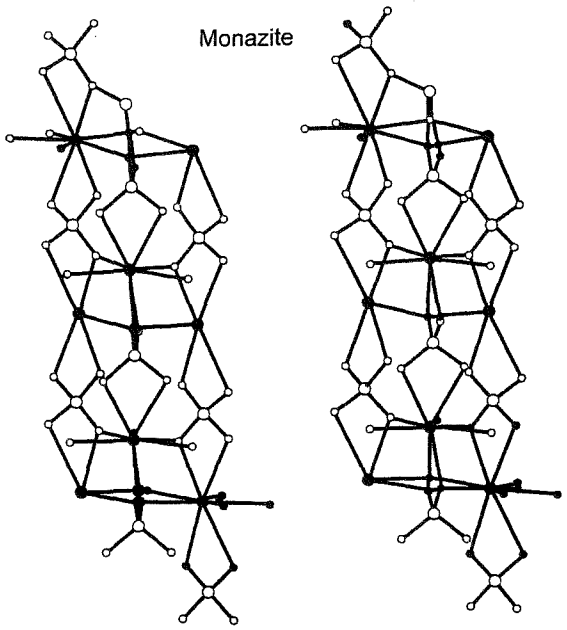


**Figure 14.** The chain-like nature and interlocking mechanism of the monoclinic monazite structure illustrates the apical linking that forms the chains, shown in a stereo view. The large open circles represent phosphorous while the large solid circles represent the rare-earth ions. The small open circles represent oxygen (after Mullica et al. 1985a,b).

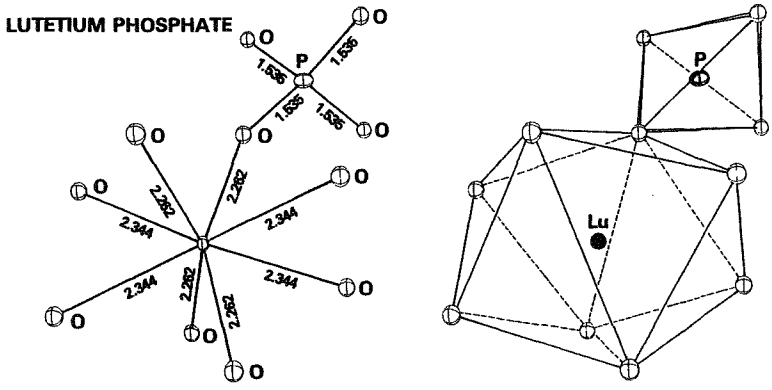


**Figure 15.** (Left) The eight-fold coordination of lutetium in the tetragonal-symmetry structure of $Lu(PO_4)$ is illustrated. As shown, there are four Lu-O bonds with a length of 2.344 Å and four Lu-O bonds with a length of 2.262 Å. (Right) The distorted dodecahedron $D_{2d}$ described by Milligan et al. (1983).

inter-chain distances exhibit a regular variation with the rare-earth Z value. Two different RE-phosphorous distances occur in the case of the monazite structure and only one distance occurs for the xenotime structure. The variation of the RE-phosphorous distances with the RE element radius is shown in Figure 17 (after Ni et al. 1995).

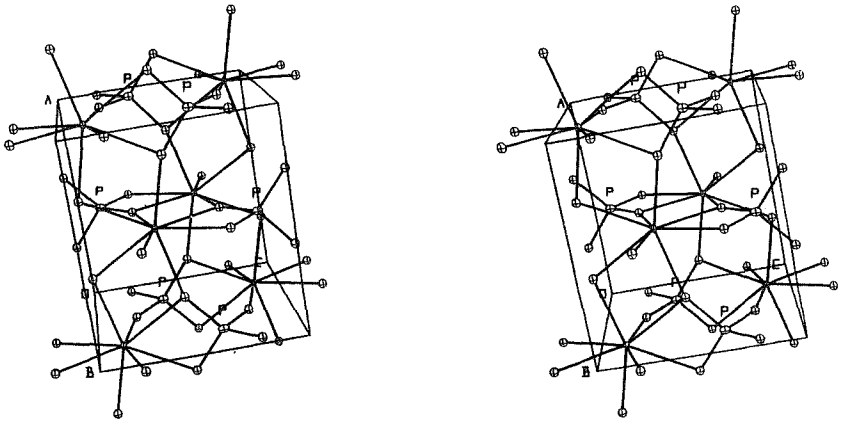

**Figure 16.** The details of the molecular packing in a tetragonal-structure orthophosphate are shown in a stereo view that illustrates the nature of the linkage between RE-O structural units (after Milligan et al. 1982).

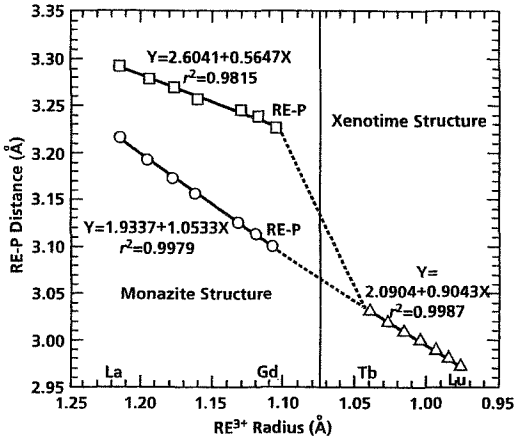


**Figure 17.** The variation of the RE-to-phosphate distances is shown as a function of the RE-ion radius for both the monazite- and xenotime-structure orthophosphate compounds. As shown in this figure, the shorter RE-to-phosphorous distances in the monoclinic structure compounds vary linearly with the trivalent RE ion radius with a slope that is close to 1. A similar variation is evident for the RE-P distances in the tetragonal xenotime-structure compounds—a trend that supports the comparison of the [001] polyhedron-$PO_4$ tetrahedron "chain arrangement" in the two structural types (after Ni et al. 1995).

A chain-like structure similar to that exhibited by the monoclinic orthophosphates is also found for the tetragonal zircon type materials. Each of these structure types has four chains in each unit cell, with the principal difference between the xenotime and monazite structural types residing in the difference in the coordination number. The linking of the chains occurs laterally through edge-sharing of adjacent polyhedra (Ni et al. 1995). One view of how the RE ions link to the $PO_4$ tetrahedral units in the xenotime structure is provided by the stereo view of $Y(PO_4)$ looking down the *c* axis of the structure shown in

Figure 18. The relationship between the monazite and xenotime structures has been described in detail by Ni et al. (1995). These workers point out that the two structures are related by a shift of the (100) planes along [010] by 2.23 Å and 1/2 $a \cos\beta$ = 0.79 Å along [001], plus a small rotation of the tetrahedron about [001].

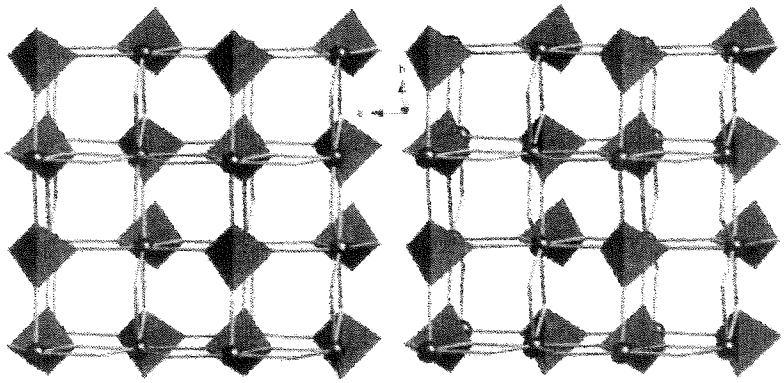

**Figure 18.** A stereo view looking down the *c*-axis is shown for the xenotime structure, i.e., of $Y(PO_4)$. This illustrates the three-dimensional nature of the vertical and lateral linkage between the structural units.

The structural properties of several mixed RE-orthophosphates were also investigated by Mullica et al. (1986, 1990, 1992, 1996). In the case of 1:1 Gd/Yb orthophosphate (Mullica et al. 1986), the structure was found to be of the tetragonal zircon structure type with $a$ = 6.865(2) Å, $c$ = 6.004(2) Å, and unit cell volume = 283.0(3) $Å^3$. Structural refinements were also carried out for Gd/Er-, Gd/Y-, and Gd/Yb-orthophosphates with a 1:1 RE ratio and for $(Gd/Yb)PO_4$ and with a 75:25 ratio of Gd toYb (Mullica et al. 1990). The mixed systems 1:1 $(Gd/Tb)PO_4$, 3:1$(Gd/Tb)PO_4$ and 9:1 $(Lu/Tb)PO_4$ were also investigated (Mullica et al. 1992) as were seven mixed compounds in the (Ce/Tb), (Nd/Tb), and $(Sm/Tb)PO_4$ families of orthophosphates (Mullica et al. 1996). All of the mixed orthophosphates investigated by Mullica et al. were found to crystallize with the tetragonal zircon structure. At this time, a considerable body of structural and crystal chemical data exists for the synthetic RE, Y, and Sc orthophosphates as evidenced by the previously cited references of Mullica et al., Milligan et al., and Ni et al. to which the reader is referred for details. Additionally the related structural investigations of Chakoumakos et al. (1994) should be noted. In these studies, structural refinements of the zircon-type RE-, Y-, and Sc-orthovanadates are reported.

## PHYSICAL, OPTICAL, AND SOLID-STATE CHEMICAL PROPERTIES

The solid-state chemical, optical, and physical properties of the RE, Y, and Sc orthophosphates have been extensively investigated by means of numerous techniques. Such studies include optical spectroscopy (Trukhin and Boatner 1997), x-ray absorption (Shuh et al. 1994), electron paramagnetic resonance (EPR) spectroscopy (Abraham et al. 1981, Boatner et al. 1981b), Mössbauer (Huray et al. 1982), Rutherford backscattering (Sales et al. 1983), and other techniques. Additionally, scanning ellipsometry has been used by Jellison and Boatner (2000) to determine the spectroscopic refractive indices of the xenotime–structure RE orthophosphates. The extensive range of studies of these orthophosphates was motivated initially by the potential application of the ortho-phosphates to radioactive waste disposal and subsequently by the other applications

discussed previously in this chapter. In addition to the motivation provided by existing and potential applications, the RE, Y, and Sc orthophosphates have proven to be versatile hosts (or actual subjects in their own right in the pure form) for numerous basic scientific studies of rare-earth electronic, phonon, and magnetic properties.

Numerous studies of the solid-state chemical properties of the RE-, Y-, and Sc-orthophosphates have been performed using EPR techniques. These investigations have shed considerable light on the ability of the orthophosphates to incorporate a diverse range of cation impurities encompassing other rare-earth ions, iron-group ions, actinide impurities, and other impurities such as Hf and Zr. EPR studies of a variety of rare-earth impurities in the tetragonal hosts $Lu(PO_4)$, $Y(PO_4)$, and $Sc(PO_4)$ were carried out by Abraham et al. (1983). A representative EPR spectrum showing the EPR signals from isotopically enriched $^{145}Nd^{3+}$ as well as EPR lines due to $Gd^{3+}$ and $Er^{3+}$ is shown in Figure 19. Results such as these illustrate the solid-state chemical capability of incorporating many combinations of RE impurities in various orthophosphate hosts. The EPR method is applicable to the study of the solid-state chemistry of paramagnetic species in both orthophosphate single crystals and powders or ceramics. Figure 20 shows an example of the ERP spectra of a $Gd^{3+}$ impurity in both single crystals and powders of synthetic xenotime (Rappaz et al. 1980).

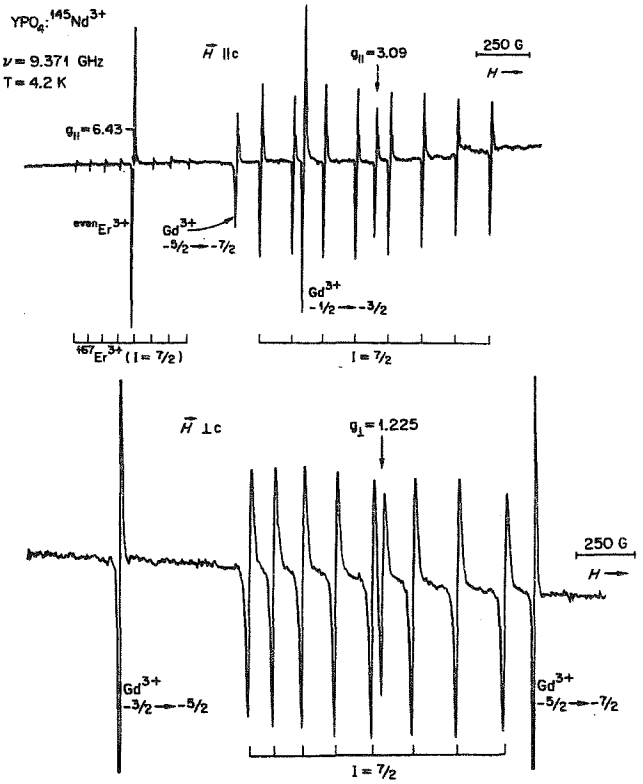


**Figure 19.** X-band EPR spectra (at T = 4.2 K) showing the hyperfine structure due to $Nd^{3+}$ (isotopically enriched with $^{145}Nd$). The spectra are shown for the applied magnetic field oriented parallel and perpendicular to the *c*-axis of the $Y(PO_4)$ host single crystal. The EPR spectrum of $Er^{3+}$ and lines from the spectrum of $Gd^{3+}$ are also present. This type of magnetic resonance spectroscopy has proven to be very useful in the study of the solid-state chemical properties of the rare-earth-, Y-, and Sc-orthophosphates (after Abraham et al. 1983).

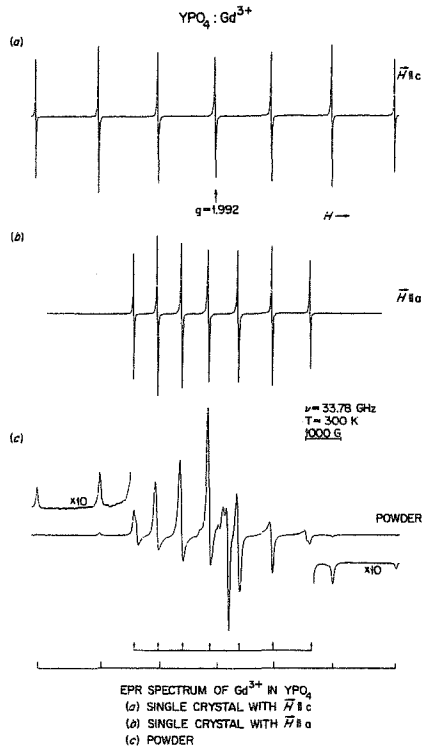


**Figure 20.** X-band EPR spectra of both single crystals and powders of $Y(PO_4)$ doped with $Gd^{3+}$ are shown. The single-crystal $Gd^{3+}$ spectra are shown for both the parallel and perpendicular orientations of the applied magnetic field relative to the c-axis of the $Y(PO_4)$ crystal. The powder spectrum of $Gd^{3+}$ shown at the bottom of the figure represents an effective geometrical average of the EPR transitions over all possible orientations of the numerous $Y(PO_4)$ powder grains (after Rappaz et al. 1980).

One of the more intriguing aspects of the solid-state chemical characteristics of synthetic xenotime, pretulite, and $Lu(PO_4)$ was revealed by EPR techniques. In the work of Abraham et al. (1984, 1985, 1986), EPR spectroscopy was used to identify the unusual $3^+$ valence state of Zr, Ti, and Hf impurities incorporated in the noted orthophosphate hosts. In the case of Zr and Ti, the trivalent state was observed as a stable valence state that existed in some as-grown crystals (i.e. stable at room temperature and above). In the case of $Hf^{3+}$ it was necessary to gamma irradiate the Hf-doped crystals at 77 K and to maintain the samples at that temperature during the EPR observations. Figure 21 shows the room temperature EPR spectrum of a single crystal of $Sc(PO_4)$ doped with isotopically enriched $^{91}Zr^{3+}$. Trivalent iron-group impurities other than $Ti^{3+}$ can be readily incorporated in the subject orthophosphates as evidenced by the study of $Fe^{3+}$ in $Y(PO_4)$, $Sc(PO_4)$, and $Lu(PO_4)$ reported by Rappaz et al. (1982). Divalent iron group impurities can also be incorporated in the Re, Y, and Sc orthophosphates as illustrated by case of $Mn^{2+}$ impurities in these tetragonal hosts (Boldu et al. 1985).

Several basic investigations of the spectroscopic properties of REs, either in the form of the pure compound or as impurities doped into hosts [$Y(PO_4)$, $Sc(PO_4)$, and $Lu(PO_4)$ in particular], have been performed. Raman spectra for the orthophosphates were reported by Begun et al. (1981), and other more-detailed investigations employing Raman spectroscopy were carried out by Becker et al. (1984, 1985, 1986, 1992) and by Williams et al. (1989a,b,c). Optical spectroscopic studies of Pr, Nd, and Er have been reported by Hayhurst et al. (1981, 1982), and studies of $Ce^{3+}$ in $Lu(PO_4)$ and $Y(PO_4)$ by Sytsma et al. (1993). Magnetic transitions in $Tb(PO_4)$ have been investigated by Liu et al. (1994). Neutron scattering and diffraction techniques have been applied to studies of the ground-state properties of pure rare-earth orthophosphate compounds by Loong et al.

(1993a,b,c; 1994, 1999), and the lattice dynamics of $Lu(PO_4)$ were investigated by Nipko et al. (1997a,b). Anomalous temperature-induced variations in the lattice parameters of $Ho(PO_4)$ and $Ho(VO_4)$ were reported by Skanthakumar et al. (1995).

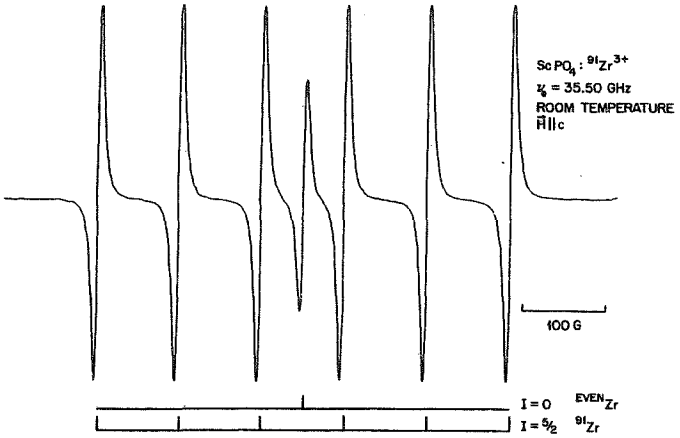


**Figure 21.** Room temperature EPR spectrum of a $^{91}Zr^{3+}$ (isotopically enriched) impurity in synthetic pretulite. The observation of unusual valence states like $Zr^{3+}$ and $Hf^{3+}$, some of which are stable in the as-grown single crystals, represents an unusual feature of the solid state chemical properties of the xenotime-structure orthophosphates (after Abraham et al. 1984).

## SUMMARY

The properties and applications of orthophosphates formed from the light and heavy rare-earth elements and from yttrium and scandium continue to represent important research topics in the fields of geology, geochronology, radioactive waste disposal, ceramic composites, gamma-ray scintillators, and a variety of optical devices. As discussed in the preceding sections, these are remarkable materials that are characterized by an unusual combination of chemical, physical, radiation-response, mineralogical, and other properties. Interest in these intriguing materials continues to grow, and undoubtedly, the future will witness a wide range of new investigations that will both further enlighten us in regard to the fundamental aspects of these materials and lead to the identification of new applications and to the development of new devices.

## ACKNOWLEDGMENTS

This chapter is dedicated to Donald F. Mullica—a loyal colleague—who was professionally committed to the science of crystallography and personally committed to the welfare of his students and his friends. The able and tireless assistance of Joanne Ramey in many aspects of this work is gratefully acknowledged, as is the assistance of J. Matt Farmer for his help in the preparation of a number of the crystal-structure illustrations. This research was sponsored by the Division of Materials Sciences, Office of Basic Energy Sciences, United States Department of Energy under contract DE-AC05-00OR22725. Oak Ridge National Laboratory is managed and operated by UT-Battelle, LLC.

## REFERENCES


Abraham MM, Boatner LA (1982) Electron-paramagnetic-resonance investigations of $^{243}Cm^{3+}$ in $LuPO_4$ single crystals. Phys Rev B 26:1434-1437

Abraham MM, Boatner LA, Rappaz M (1980a) Novel measurement of hyperfine interactions in solids: $^{207}Pb^{3+}$ in $YPO_4$ and $LuPO_4$. Phys Rev Letters 45:839-842

Abraham MM, Boatner LA, Quinby TC, Thomas DK, Rappaz M (1980b) Preparation and compaction of synthetic monazite powders. Radioactive Waste Management 1:181-191

Abraham MM, Boatner LA, Rappaz M (1981) EPR investigations of impurities in the lanthanide orthophosphates. *In* Nuclear and Electron Resonance Spectroscopies Applied to Materials Science. Kaufmann EN, Shenoy GK (ed) Elsevier North-Holland, p 475-480

Abraham MM, Boatner LA, Ramey JO, Rappaz M (1983) An EPR study of rare-earth impurities in single crystals of the zircon-structure orthophosphates $ScPO_4$, $YPO_4$, and $LuPO_4$. J Chem Phys 78:3-10

Abraham MM, Boatner LA, Ramey JO, Rappaz M (1984) The occurrence and stability of trivalent zirconium in orthophosphate single crystals. J Chem Phys 81:5362-5366

Abraham MM, Boatner LA, Ramey JO, (1985) The observation by EPR of trivalent hafnium in $LuPO_4$, $YPO_4$, and $ScPO_4$. J Chem Phys 83:2754-2758

Abraham MM, Boatner LA, Aronson MA (1986) EPR observations of trivalent titanium in orthophosphate single crystals. J Chem Phys 85:1-6

Abraham MM, Boatner LA, Finch CB, Kot W, Conway JG, Shalimoff GV, Edelstein NM, (1987) EPR and optical-absorption studies of $Cm^{3+}$ in $YPO_4$ and $LuPO_4$ single crystals. Phys Rev B – Condens Matter 35:3057-3061

Allison SW, Boatner LA, Gillies GT (1995) Characterization of high-temperature thermographic phosphors: spectral properties of $LuPO_4$:Dy(1%), Eu(2%). Appl Opt 34:5624-5627

Allison SW, Cates MR, Gillies GT, Boatner LA (1998) High temperature thermometric phosphors for use in a temperature sensor. U.S. Patent 5,730,528

Allison SW, Cates MR, Boatner LA, Gillies GT (1999) High temperature thermometric phosphors. U.S. patent 5,885,484

Andrehs G and Heinrich W (1998) Experimental determination of REE distributions between monazite and xenotime: potential for temperature-calibrated geochronology. Chemical Geology 149:83-96

Bamberger CE (1982) Preparation of metal phosphates by metathesis reaction with $BPO_4$. J Am Ceram Soc 65:C107-C108

Bamberger CE, Haire RG, Hellwege HE, and Begun GM (1984) Synthesis and characterization of crystalline phosphates of plutonium(III) and plutonium(IV). J Less-Common Metals 97:349-356

Bea F, Periera MD, Corretge LG, Fershtater GB (1994) Differentiation of strongly peraluminous perphosphorous granites: The Pedrobernardo pluton, central Spain. Geochim Cosmochim Acta 58:2609-2627

Bea F (1996) Residence of REE, Y, Th and U in granites and crystal protoliths: Implications for the chemistry of crystal melts. J Pet 37:521-552

Beall GW, Boatner LA, Mullica DF, Milligan WO (1981) The structure of cerium orthophosphate, a synthetic analog of monazite. J Inorg Nucl Chem 43:101-105

Becker P, Hayhurst T, Shalimoff G, Conway JG, Edelstein N, Boatner LA, Abraham MM (1984) Crystal field analysis of $Tm^{3+}$ and $Yb^{3+}$ in $YPO_4$ and $LuPO_4$. J Chem Phys 81:2872-2878

Becker PC, Williams GM, Edelstein N, Bucher JJ, Russo RE, Koningstein JA, Boatner LA, Abraham MM (1985) Intensities and asymmetries of electronic Raman scattering in $ErPO_4$ and $TmPO_4$. Phys Rev B 31:8102-8110

Becker PC, Williams GM, Edelstein N, Koningstein JA, Boatner LA, Abraham MM (1986) Resonance electronic Raman scattering in erbium phosphate crystals. Optics Lett 11:282-284.

Becker PC, Williams GM, Edelstein NM, Koningstein JA, Boatner LA, Abraham MM (1992) Observation of strong electron-phonon coupling effects in $YbPO_4$. Phys Rev B - Condens Matter 45:5027-5030

Begun GM, Beall GW, Boatner LA, Gregor WT (1981) Raman spectra of the rare earth orthophosphates. J Raman Spectrosc 11:273-278

Bernhard F, Walter F, Ettinger K, Taucher J, Mereiter K (1998) Pretulite, $ScPO_4$, a new scandium mineral from the Styrian and lower Austrian lazulite occurrences, Austria. Am Mineral 83:625-630

Boatner LA, Sales BC (1988) Monazite. *In* Radioactive Waste Forms for the Future. Lutze W, Ewing RC (eds) Elsevier North-Holland, Amsterdam, Ch 8

Boatner LA, Beall GW, Abraham MM, Finch CB, Huray PG, Rappaz M (1980) Monazite and other lanthanide orthophosphates as alternate actinide waste forms. *In* Scientific Basis for Nuclear Waste Management. Northrup CJ (ed) Plenum Publishing, New York, p 289-296

Boatner LA, Beall GW, Abraham MM, Finch CB, Floran RJ, Huray PG, Rappaz M (1981a) Lanthanide orthophosphates for the primary immobilization of actinide wastes. *In* Management of Alpha-Contaminated Wastes. Intl Atomic Energy Agency, Vienna (IAEA-SM246/73), p 411-422

Boatner LA, Abraham MM, Rappaz M (1981b) The characterization of nuclear waste forms by EPR spectroscopy. *In* Scientific Basis for Nuclear Waste Management. Moore JG (ed) Plenum Publishing, New York, p 181-188

Boatner LA, Abraham MM, Sales BC (1983) Lanthanide orthophosphate ceramics for the disposal of actinide-contaminated nuclear wastes. Inorganica Chimica Acta 94(E23):146

Boldú JL, Muñoz E, Abraham MM, Boatner LA (1985) EPR and thermoluminescence investigations of $Mn^{2+}$ in $LuPO_4$, $YPO_4$, and $ScPO_4$. J Chem Phys 83:6113-6120

Bondar IA, Domanskii AI, Mezentseva LP, Degen MG, Kalinina NE (1976) A physicochemical study of lanthanide orthophosphates. Russ J Inorg Chem (Engl. Transl.) 21:1126-28

Carron MK, Mrose ME, Murata KJ (1958) Relation of ionic radius to structures of rare-earth phosphates, arsenates, and vanadates. Am Mineral 43:985-989

Chakoumakos BC, Abraham MM, Boatner LA (1994) Crystal structure refinements of zircon-type $MVO_4$ (M = Sc, Y, Ce, Pr, Nd, Tb, Ho, Er, Tm, Yb, Lu). J Solid State Chem 109:197-202

Donovan JJ, Hanchar JM, Picolli PM, Schrier MD, Boatner LA, Jarosewich E (2002a) A re-examination of the rare-earth element orthophosphate reference samples for electron microprobe analysis. Can Mineral, submitted for publication.

Donovan JJ, Hanchar JM, Picolli P, Schrier MD, Boatner, LA (2002b) Contamination in the rare-earth-element orthophosphate reference samples. NIST J Res (submitted)

Eigermann W, Müller-Vogt G, Wendl W (1978) Solubility curves in high-temperature melts for the growth of single crystals of rare earth vanadates and phosphates. Phys Stat Sol (a) 49:145-148

Ewing RC (1975) The crystal chemistry of complex niobium and tantalum oxides. IV. The metamict state. Am Mineral 60:728-733

Ewing RC, Haaker RF (1980) The metamict state: Implications for radiation damage in crystalline waste forms. Nucl Chem Waste Management 1:51-57

Eyal Y and Kaufman A (1982) Alpha-recoil damage in monazite: preferential dissolution of the radiogenic actinide isotopes. Nuclear Technology 58:77-83

Eyal Y and Fleischer RL, (1985) Preferential leaching and the age of radiation damage from alpha decay in minerals. Geochim Cosmochim Acta 48:1155-1164

Feigelson RS (1964) Synthesis and single crystal growth of rare-earth orthophosphates. J Am Ceram Soc 47:257-258

Floran RJ, Abraham MM, Boatner LA, Rappaz M (1981a) Geologic stability of monazite and its bearing on the immobilization of actinide wastes. *In* Scientific Basis for Nuclear Waste Management. Moore JG (ed) Plenum Publishing, New York, p 507-514

Floran RJ, Rappaz M, Abraham MM, Boatner LA (1981b) Hot and cold pressing of $(La,Ce)PO_4$-based nuclear waste forms. *In* Alternate Nuclear Waste Forms and Interactions in Geologic Media. Boatner LA, Battle GC (ed) USDOE CONF-8005107 p 185-193

Förster H-J (1998a) The chemical composition of REE-Y-Th-U-rich minerals in peraluminous granites of the Erzgebirge-Fichtelgebirge region, Germany, Part I: The monazite-(Ce)-brabanite solid solution series. Am Mineral 83:259-272

Förster H-J (1998b) The chemical composition of REE-Y-Th-U-rich accessory minerals in peraluminous granites of the Erzgebirge-Fichtelgebirge region, Germany. Part II: Xenotime. Am Mineral 83: 1302-1315

Ghouse KM (1968) Refinement of the crystal structure of heat-treated monazite crystal. Indian J Pure Appl Phys 6:265-268

Von Gliszcynski S (1939) Beitrag zur isomorphis von monazit und krokoit. Z Kristallogr 101:1-16

Gramaccioli CM, Segalstad TU (1978) A uranium- and thorium-rich monazite from a south-alpine pegmatite at Piona, Italy. Am. Mineral. 63:757-761

Gratz R, Heinrich W (1997) Monazite-xenotime thermobarometry: Experimental calibration of the miscibility gap in the binary system $CePO_4$-$YPO_4$. Am Mineral 82:772-780

Hayhurst T, Shalimoff G, Edelstein N, Boatner LA, Abraham MM (1981) Optical spectra and Zeeman effect for $Er^{3+}$ in $LuPO_4$ and $HfSiO_4$. J Chem Phys 74:5449-5452

Hayhurst T, Shalimoff G, Conway JG, Edelstein N, Boatner LA, Abraham (1982) Optical Spectra and Zeeman effect for $Pr^{3+}$ and $Nd^{3+}$ in $LuPO_4$ and $YPO_4$. J Chem Phys 76:3960-3966

Heinrich W, Andrehs G. and Franz G (1997) Monazite-xenotime miscibility gap thermometer: I. An empirical calibration. J Metamorph Geol 15:3-16

Hikichi Y (1991) Synthesis of monazite ($RPO_4$, R = La, Ce, Nd, or Sm) by solid state reaction. Mineral J 15:268-275

Hikichi Y, Nomura T (1987) Melting temperatures of monazite and xenotime. J Am Ceram Soc 70: C-252–C-253

Hikichi Y, Hukuo K, Shiokawa J (1978) Synthesis of rare earth orthophosphates. Bull Chem Soc Jpn 51:3645-3646

Hikichi Y, Hukuo K, Shiokawa J (1980) Solid state reactions between rare earth orthophosphate and oxide. Bul. Chem Soc Jpn 53:1455-1456

Hikichi Y, Sasaki T, Suzuki S, Murayama K (1988) Thermal reactions of hydrated hexagonal $RPO_4 \cdot nH_2O$ (R = Tb or Dy, n = 0.5 to 1). J Am Ceram Soc 71:C-354–C-355

Hikichi Y, Sasaki T, Murayama K, Nomura T (1989) Mechanochemical changes of weinschenkite-type $RPO_4 \cdot 2H_2O$ [R = Dy, Y, Er, or Yb] by grinding and thermal reactions of the ground specimens. J Am Ceram Soc 72:1073-1076

Hikichi Y, Yu CF, Miyamoto M, Okada S (1991) Mechanical conversion of rhabdophane type $RPO_4 \cdot nH_2O$ (r = La, Ce, Pr, Nd or Sm, n~1/2) to the monazite type analogues. Mineral J 15:349-355

Hikichi Y, Yu CF, Miyamoto M, Okada S (1993) Mechanochemical changes in hydrated rare earth orthophosphate minerals by grinding. J Alloys Comp 192:102-104

Hikichi Y, Yogi K, Ota T (1995) Preparation of rhabdophane-type $RPO_4 \cdot nH_2O$ (R = Y or Er, n = 0.7-0.8) by pot-milling churchite-type $RPO_4 \cdot 2H_2O$ at 20-25°C in air. J Alloys Comp 224:L1-L3

Hikichi Y, Ota T, Hattori T Imaeda T (1996) Synthesis and thermal reactions of rhabdophane = (Y). Mineral J 18:87-96

Hinton RW and Paterson BA (1994) Crystallization history of granitic magma: Evidence from trace element zoning. Mineral Mag 58A:416-417

Hintzmann W, Müller-Vogt G (1969) Crystal growth and lattice parameters of rare-earth doped yttrium phosphate, arsenate and vanadate prepared by the oscillating temperature flux technique. J Cryst Growth 5:274-278

Houk LG (1943) Monazite Sand. Information Circular 7233, U S Department of the Interior – Bureau of Mines

Huray PG, Spaar MT, Nave SE, Legan JM, Boatner LA, Abraham MM (1982) The Application of $^{57}Fe$ Mössbauer spectroscopy to the characterization of nuclear waste forms. *In* Scientific Basis for Nuclear Waste Management. Topp SV (ed) Elsevier, North Holland, p 59-66

Jarosewich E and Boatner LA (1991) Rare-earth element reference samples for electron microprobe analysis. Geostandards Newsletter 15:397-399

Jellison GE, Boatner LA (2000) Spectroscopic refractive indices of metal-orthophosphates with the zircon type structure. Opt Mater 15:103-109

Johnstone SJ (1914) Monazites from some new localities. J Chem Industry 33:55-59

Jonasson RG and Vance ER (1986) DTA study of the Rhabdophane to monazite transformation in rare earth (La–Dy phosphates. Thermochemica Acta 108:65-72

Jonasson RG, Bancroft GM, Boatner LA (1988) Surface reactions of synthetic, end-member analogues of monazite, xenotime and rhabdophane, and evolution of natural waters. Geochim Cosmochim Acta 52:767-770

Kato T (1958) A study on monazite from the Ebisu mine, Gifu prefecture. Mineral J (Japan) 2:224

Kelly KL, Beall GW, Young JP, Boatner LA (1981) Valence states of actinides in synthetic monazites. *In* Scientific Basis for Nuclear Waste Management. Moore JG (ed) Plenum Publishing, New York, p 189-195

Kizilyalli M and Welch AJE (1976) Crystal data for lanthanide orthophosphates. J Appl Crystallogr 9: 413-414

Kot WK, Edelstein NM, Abraham MM, Boatner LA (1993a) Zero-field splitting of $Cm^{3+}$ in $LuPO_4$ single crystals. Phys Rev B 48:12704-12712

Kot WK, Edelstein NM, Abraham MM, Boatner LA (1993b) Electron paramagnetic resonance of $Pu^{3+}$ and $Cf^{3+}$ in single crystals of $LuPO_4$. Phys Rev B 47:3412-3414

Lempicki A, Berman E, Wojtowicz AJ, Balcerzyk M, Boatner LA (1993) Cerium-doped orthophosphates: new promising scintillators. IEEE Trans Nucl Sci 40:384-387

Liu GK, Loong CK, Trouw F, Abraham MM, Boatner LA (1994) Spectroscopic studies of magnetic transitions in $TbPO_4$. J Appl Phys 75:7030-7032

Liu GK, Li ST, Zhorin VV, Loong CK, Abraham MM, Boatner LA (1998) Crystal-field splitting, magnetic interaction, and vibronic excitations of $^{244}Cm^{3+}$ in $YPO_4$ and $LuPO_4$. J Chem Phys 109: 6800-6808

Loong CK, Soderholm AL, Abraham MM, Boatner LA, Edelstein NM (1993a) Crystal-field excitations and magnetic properties of $TmPO_4$. J Chem Phys 98:4214-4222

Loong CK, Soderholm AL, Hammonds JP, Abraham MM, Boatner LA (1993b) Neutron study of crystal-field transitions in $ErPO_4$. J Appl Phys 73:6069-6071

Loong CK, Soderholm L, Goodman GL, Abraham MM, Boatner LA (1993c) Ground-state wave functions of $Tb^{3+}$ ions in paramagnetic $TbPO_4$: a neutron scattering study. Phys Rev B 48:6124-6131

Loong CK, Soderholm L, Xue JS, Abraham MM, Boatner LA (1994) Rare earth energy levels and magnetic properties of $DyPO_4$. J Alloys Comp 207/208:165-169

Loong CK, Loewenhaupt M, Nipko JC, Braden M, Reichardt W, Boatner LA (1999) Dynamic coupling of crystal-field and phonon states in $YbPO_4$. Phys Rev B 60:R12549-R12552

Marinova LA and Yaglov VN (1976) Thermodynamic characteristic of lanthanide phosphates. Russ J Physical Chem 50:477 (Translated from: Zh Fizicheskoi Khimi 50:802-803)

Marshall DB, Morgan PED, Housley RM (1997) Debonding in multilayered composites of zirconia and $LaPO_4$. J Am Ceram Soc 80:1677-1683

Marshall DB, Morgan PED, Housley RM, Cheung JT (1998) High-temperature stability of the $Al_2O_3$-$LaPO_4$ system. J. Am. Ceram. Soc. 81:951-956

McCarthy GJ, White WB, Pfoertsch DE, (1978) Synthesis of nuclear waste monazites, ideal actinide hosts for geological disposal. Mater Res Bull 13:1239-1245

Meldrum A, Boatner LA, Ewing RC (1997a) Displacive radiation effects in the monazite- and zircon-structure orthophosphates. Phys Rev B 56:13805-13814

Meldrum A, Boatner LA, Ewing RC (1997b) Electron-irradiation-induced nucleation and growth in amorphous $LaPO_4$ and $ScPO_4$, and zircon. J Mater Res 12:1816-1827

Meldrum A, Boatner LA, Wang LM, Ewing RC (1997c) Ion-beam-induced amorphization of $LaPO_4$ and $ScPO_4$. Nucl Instrum Methods Phys Res B 127/128:160-165

Meldrum A, Boatner LA, Weber WJ, Ewing RC (1998) Radiation damage in zircon and monazite. Geochim Cosmochim Acta 62:2509-2520

Meldrum A, Boatner LA, Ewing RC (2000) A comparison of radiation effects in crystalline $ABO_4$-type phosphates and silicates. Mineral Mag 64:185-194

Milligan WO, Mullica DF, Beall GW, Boatner LA (1982) Structural investigations of $YPO_4$, $ScPO_4$, and $LuPO_4$. Inorganica Chimica Acta 60: 39-43

Milligan WO, Mullica DF, Beall GW, Boatner LA (1983a) The structures of three lanthanide orthophosphates. Inorganica Chimica Acta 70:133-136

Milligan WO, Mullica DF, Beall GW, Boatner LA (1983b) Structures of $ErPO_4$, $TmPO_4$, and $YbPO_4$. Acta Crystallogr C 39:23-24

Milligan WO, Mullica DF, Perkins HO, Beall GW, Boatner LA (1983c) Crystal data for lanthanide orthophosphates with the zircon-type structure. Inorganica Chimica Acta 77:L23-L25

Mooney RCL (1948) Crystal structures of a series of rare earth phosphates. J Chem Phys 16:1003

Mooney RCL (1950) X-ray diffraction study of cerous phosphate and related crystals. I. Hexagonal modification. Acta Crystallogr 3:337-340

Morgan PED and Marshall DB (1993) Functional interfaces for oxide/oxide composites. Mater Sci Engin A162:15-25

Morgan PED and Marshall DB (1995) Ceramic composites of monazite and alumina. J Am Ceram Soc 78:1553-1563

Morgan PED and Marshall DB (1996) Ceramic composites having a weak bond material selected from monazites and xenotimes. U.S. patent 5,514,474

Morgan PED and Marshall DB (1997) Fibrous composites including monazites and xenotimes. U.S. Patent 5,665,463

Moses WW, Weber MJ, Derenzo SE, Perry D, Berdahl P, Schwarz L, Sasum U, Boatner LA (1997) Recent results in a search for inorganic scintillators for X- and gamma-ray detection. Proc Intl Conf Inorganic Scintillators and Their Applications. Chinese Academy of Sciences Press, Shanghai, China p 358-361

Moses WW, Weber MJ, Derenzo SE, Perry D, Berdahl P, and Boatner LA (1998) Prospects for dense, infrared emitting scintillators. IEEE Trans on Nucl Sci 45:462-466

Mullica DF, Milligan WO, Grossie DA, Beall GW, Boatner LA (1984) Nine-fold coordination in $LaPO_4$: pentagonal interpenetrating tetrahedral polyhedron. Inorganica Chimica Acta 95:231-236

Mullica DF, Grossie DA, Boatner LA (1985a) Structural refinements of praseodymium and neodymium orthophosphate. J Solid State Chem 58:71-77

Mullica DF, Grossie DA, Boatner LA (1985b) Coordination geometry and structural determinations of $SmPO_4$, $EuPO_4$, and $GdPO_4$. Inorganica Chimica Acta 109:105-110

Mullica DF, Grossie DA, Boatner LA (1986) Crystal structure of 1:1 gadolinium/ytterbium orthophosphate. Inorganica Chimica Acta 118:173-176

Mullica DF, Sappenfield EL, Wilson GA, Boatner LA (1989) The crystal structure of $Ce_{0.9}U_{0.1}PO_4$. Lanthanide Actinide Res 3:51-61

Mullica DF, Sappenfield EL, Boatner LA (1990) A structural investigation of several mixed lanthanide orthophosphates. Inorganica Chemica Acta 174:155-159

Mullica DF, Sappenfield EL, Boatner LA (1992) Single-crystal analysis of mixed ($Ln/TbPO_4$) orthophosphates. J Solid State Chem 99:313-318

Mullica DF, Sappenfield EL, Boatner LA (1996) Monazite-and zircon-type structures of seven mixed $(Ln/Ln)PO_4$ compounds. Inorganica Chimica Acta 244:247-252

Murdoch KM, Edelstein NM, Boatner LA, Abraham MM (1996) Excited state absorption and fluorescence line narrowing studies of $Cm^{3+}$ in $LuPO_4$. J Chem Phys 105:2539-2546

Muto T, Meyrowitz R. Pommer AM, Murano T (1959) Ningyoite, a new uranous phosphate mineral from Japan. Am Mineral 44:633-650

Ni Y, Hughes JM, and Mariano AN (1995) Crystal chemistry of the monazite and xenotime structures. Am Mineral 80:21-26

Nipko JC, Loong CK, Loewenhaupt M, Braden M, Reichart W, Boatner LA (1997a) Lattice dynamics of xenotime: The phonon dispersion relations and density of states of $LuPO_4$. Phys Rev B 56: 11584-11592

Nipko JC, Loong CK, Loewenhaupt M, Reichardt W, Braden M, Boatner LA (1997b) Lattice dynamics of $LuPO_4$. J Alloys Comp 250:573-576

Orlovskii VP, Khalikov BS, Bugakov VI, and Kurbanov KhM (1975) Conditions for transfer and formation of single crystals of $HoPO_4$. Izvestiya Akademii Nauk SSSR, Neorganicheskie Materialy 11:494-497

Parish W (1939) Unit cell and space group of monazite (LaCe:Y)$PO_4$. Am Mineral 24:651-652

Pasteels P (1970) Uranium-lead radioactive ages of monazite and zircon from the Vire-Caroles granite (Normandy): A case of zircon-monazite discrepancy. Eclogae Geol Helv 63:231-237

Penfield SC (1882) Sand from Brindletown district, Burke County, NC. Am J. Sci. 24:252

Pepin JG and Vance ER (1981) Crystal data for rare-earth orthophosphates of the monazite structure type. J Inorg Nucl Chem 43:2807-2809

Petek M, Abraham MM, Boatner LA (1982) Lanthanide orthophosphates as a matrix for solidified radioactive defense and reactor wastes. *In* Scientific Basis for Nuclear Waste Management. Topp SV (ed) Elsevier, North Holland, p 181-186

Podor R and Cuney M (1997) Experimental study of Th-bearing $LaPO_4$ (780°C, 200 MPa):Implications for monazite and actinide orthophosphate stability. Am Mineral 82:765-771

Poitrasson F, Chenery S, Bland D (1996) Contrasted monazite hydrothermal alteration mechanisms and their geochemical implications. Earth Planetary Sci Letters 145:79-96

Rapaport A, Moteau O, Bass M, Boatner L, Deka C (1999a) Optical spectroscopy and lasing properties of neodymium-doped lutetium orthophosphate. J Opt Soc Am B 16:911-916

Rapaport A, David V, Bass M, Deka C, Boatner LA (1999b) Optical spectroscopy of erbium-doped lutetium orthophosphate. J Lumin 85:155-161

Rapp RP and Watson EB (1986) Monazite solubility and dissolution kinetics: Implications for the thorium and light rare earth chemistry of felsic magmas. Contrib Mineral Petrol 94:304-316

Rapp RP, Ryerson FJ, Miller CF (1987) Experimental evidence bearing on the stability of monazite during crystal anatexis. Geophys. Res Letters 14:307-310

Rappaz M, Boatner LA, Abraham MM (1980) EPR investigations of $Gd^{3+}$ in single crystals and powders of the zircon-structure orthophosphates $YPO_4$, $ScPO_4$, and $LuPO_4$. J Chem Phys 73:1095-1103

Rappaz M, Abraham MM, Ramey JO, Boatner LA (1981a) EPR spectroscopic characterization of $Gd^{3+}$ in the monazite-type rare-earth orthophosphates: $LaPO_4$, $CePO_4$, $PrPO_4$, $NdPO_4$, $SmPO_4$, and $EuPO_4$. Phys Rev B 23:1012-1030

Rappaz M, Boatner LA, Abraham MM (1981b) The application of EPR spectroscopy to the characterization of crystalline nuclear waste forms. *In* Alternate Nuclear Waste Forms and Interactions in Geologic Media. Boatner LA, Battle GC (ed) USDOE CONF-8005107, p 185-193

Rappaz M, Ramey JO, Boatner LA, Abraham MM (1982) EPR investigations of $Fe^{3+}$ in single crystals and powders of the zircon-structure orthophosphates $LuPO_4$, $YPO_4$, and $ScPO_4$. J Chem Phys 76: 40-45

Rouanet A, Serra JJ, Allaf K, Orlovskii VP (1981) Rare earth orthophosphates at high temperatures. Izv. Akad. Nauk SSSR, Neorg Mater 17:76-81

Roy R and Vance ER (1981) Irradiated and metamict materials: relevance to radioactive waste science J. Mater Sci 16:1187-1190

Sales BC, White CW, Boatner LA (1983) A comparison of the corrosion characteristics of synthetic monazite and borosilicate glass containing simulated nuclear waste glass. Nucl Chem Waste Management 4: 281-289

von Schwarz H (1963) Die Phosphate, Arsenate und Vanadate der seltenen Erden. Z Anorgan Allgemeine Chem 323:44-56

Shuh DK, Terminello LJ, Boatner LA, Abraham MM, Perry D (1994) Characterization of Ce-doped $LaPO_4$ by x-ray absorption spectroscopy. Mater Res Soc Symp Proc Vol. 329, Materials Research Society, p. 91-96

Skanthakumar S, Loong CK, Soderholm L, Nipko J, Richardson JW Jr, Abraham, MM, Boatner LA (1995) Anomalous temperature dependence of the lattice parameters in $HoPO_4$ and $HoVO_4$: rare earth quadrupolar effects. J Alloys Compd 225:595-598

Smith SH and Wanklyn BM (1974) Flux growth of rare earth vanadates and phosphates. J Cryst Growth 21:23-28

Sytsma J, Piehler D, Edelstein NM, Boatner LA, Abraham MM (1993) Two-photon excitation of the $4f^1 \rightarrow 5d^1$ transitions of $Ce^{3+}$ in $LuPO_4$ and $YPO_4$. Phys Rev B 47:14786-14794

Sytsma J, Murdoch K, Elelstein NM, Boatner LA, Abraham MM (1995) Spectroscopic studies and crystal-field analysis of $Cm^{3+}$ and $Gd^{3+}$ in $LuPO_4$. Phys Rev B 52:12668-12676

Tanner BK and Smith SH (1975) X-ray topographic study of the perfection of flux-grown rare earth phosphates. J Cryst Growth 30:323-326

Teufel S and Heinrich W (1997) Partial resetting of the U-Pb isotope system in monazite through hydrothermal experiments: An SEM and U-Pb isotope study. Chem Geol 137:273-281

Trukhin AN, Boatner LA, (1997) Electronic structure of $ScPO_4$ single crystals: optical and photoelectric properties. Proc 13th Intl Conf Defects in Insulating Crystals. Mater Sci Forum, Transactions Technical Publications, p 239-241

Ueda T (1967) Re-examination of the crystal structure of monazite. J Jpn Assoc Mineral Petrol Econ Geol. 58:170-179

Ushakov SV, Helean KB, Navrotsky A, Boatner LA (2001) The thermochemistry of rare-earth orthophosphates. J Mater Res 16:2623-2633

Wanklyn BM (1972) Flux growth of some complex oxide materials. J Mater Science 7:813-821

Wanklyn BM (1978) Effects of modifying starting compositions for flux growth. J Cryst Growth 43: 336-344

Weigel F. Scherer V, Henschel H (1965) Unit cells of the monazite-type rare-earth phosphates. J Am Ceram Soc 48:383-384

Wickham DG (1963) Use of lead pyrophosphate as a flux for crystal growth. J Appl Phys 33:3597-98

Williams GM, Becker PC, Conway JG, Edelstein N, Boatner LA, Abraham MM (1989a) Intensities of electronic Raman scattering between crystal-field levels of $Ce^{3+}$ in $LuPO_4$: Nonresonant and near-resonant excitation. Phys Rev B 40:4132-4142

Williams GM, Becker PC, Edelstein N, Boatner LA, Abraham MM (1989b) Excitation profiles of resonance electronic Raman scattering in $ErPO_4$ crystals. Phys Rev B 40:1288-1296

Williams GM, Edelstein N, Boatner LA, Abraham MM (1989c) Anomalously small *4f-5d* oscillator strengths and *4f-4f* electronic Raman scattering cross sections for $Ce^{3+}$ in crystals of $LuPO_4$. Phys Rev B 40:4143-4152

Wisniewski D, Tavernier S, Dorenbos P, Wisniewska M, Wojtowicz AJ, Bruyndonckx P, Loef EV, Eijk CWE, Boatner LA (2002a) VUV Scintillation of $LuPO_4$:Nd and $YPO_4$:Nd. IEEE Trans Nucl Sci (submitted)

Wisniewski D, Tavernier S, Dorenbos P, Wisniewska M, Wojtowicz AJ, Bruyndonckx P, Loef EV, Eijk CWE, Boatner LA (2002b) $LuPO_4$:Nd and $YPO_4$:Nd—new promising VUV scintillation materials. Nucl Instrum Methods A, (submitted)

Wojtowicz AJ, Lempicki A, Wisniewski D, Boatner LA (1994) Cerium-doped orthophosphate scintillators. Mat Res Soc Symp Proc, Materials Research Society 348:123-129

Wojtowicz AJ, Wisniewski D, Lempicki A, Boatner LA (1995) Scintillation mechanisms in rare earth orthophosphates. *In* Radiation Effects and Defects in Solids, Vol. 135. Biersack (ed) Overseas Publishers Assoc., Amsterdam B.V., p. 305-310